A RESONANCE FLUORESCENCE MONOCHROMATOR FOR SPECTRALLY-SELECTIVE IMAGING

By

DIMITRI PAPPAS

A DISSERTATION PRESENTED TO THE GRADUATE SCHOOL OF THE UNIVERSITY OF FLORIDA IN PARTIAL FULFILLMENT OF THE REQUIREMENTS FOR THE DEGREE OF DOCTOR OF PHILOSOPHY

UNIVERSITY OF FLORIDA

2002

Για΄ την αγάπη μου, Mimi

ACKNOWLEDGEMENTS

This work would not have been possible without the support and guidance of my mentor, Jim Winefordner. He has entrusted me to develop an idea that started as a late-afternoon discussion in his office in my first semester of graduate school into a viable research project, and I hope that I have met his expectations. He has been a driving force in the direction of my career and has also been a true friend over the years. I would like to thank Jim for inspiring my interest in chemistry, and for guiding not only my graduate research but also for showing me by his example what a great scientist, teacher, advisor, and friend can be. I will always be indebted to Jim for the kindness he has shown me and for mentoring me not just in science but also in life. I will treasure the years I have spent in his laboratory.

I would also like to thank Ben Smith, whose assistance and advice have kept me going. Ben was always enthusiastic and generous with his expertise. From Ben I learned that there is an elegance and art to scientific experimentation. I will miss our discussions of antique spectroscopes and other fascinating topics, and I hope our friendship will continue long after I leave the Winefordner group.

I would like to thank my third advisor, Nicoló Omenetto, for his infectious enthusiasm. I have learned more through our scientific discussions than I ever could have from a textbook or course. Nico serves as a source of inspiration and I thank him for his guidance throughout my graduate career.

I would like to acknowledge the support of my friends and fellow students in the group, primarily Nathan Pixley, Tiffany Correll, Paige Eagan, Eric Oxley, and Ruixie Chen. Nathan and Tiffany spent their graduate careers in the lab with me and both possess the unique ability to tolerate working with me. Their contributions to this work are immeasurable, and I thank them both for the excellent science and camaraderie they provided. Igor Gornushkin and Oleg Matveev are also acknowledged for teaching me the majority of my experimental skills and always providing sound advice when I faced a difficult task. I also thank Dr. Robert Kennedy for making himself available whenever I needed advice.

I would like to acknowledge the individuals who are the infrastructure of the Department of Chemistry, and who have made my time here easier. Jeanne Karably and Sonia Simmons of the Analytical Chemistry Division office have been instrumental in making sure everything that comes in and out of the lab does so smoothly. Without their hard work I would not have research support, equipment, a stipend, publications, or this dissertation. I also thank Steve Miles and Larry Hartley of the electronics shop for teaching me everything I know about electronics. This work was supported by a grant from the National Institutes of Health and a graduate fellowship from the American Chemical Society

I would also like to thank my entire family for their support, especially my wife, Mimi. Her editorial skills and her constant support of my graduate career have made this work possible.

TABLE OF CONTENTS

ACKNOWLEDGEMENTS iii

ABSTRACT..... vii

CHAPTERS

1 AN INTRODUCTION TO NARROWBAND IMAGING 1

2 COLLISIONAL EXCITATION/IONIZATION IN CESIUM VAPOR 7

Introduction 7
Experimental Setup 8
Results and Discussion 12
Cesium dimer measurements 12
Emission of the Cs plasma 13
Current in the Cs plasma 16
Effect of the number density of Cs atoms 18
Conclusion 19

3 FLUORESCENCE MONITORING OF LASER-INDUCED POPUATION CHANGES IN CESIUM VAPOR 21

Introduction 21
Experimental Setup 23
Modeling Simulations 26
Density matrix formalism 26
Simulation results 30
Experimental Results: Fluorescence Behavior of the $6^2P^o_{3/2}$ and
$6^2P^o_{3/2}$ States 31
Conclusion 33

4 A CESIUM RESONANCE FLUORESCENCE IMAGING MONOCHROMATOR 35

Introduction 35
Experimental Setup 37

Results 41
Spectral response of the RFIM 41
Fluorescence intensity vs. photon flux 42
Two-dimensional imaging with the Cs RFIM 44
Conclusion 45

5 RESONANCE RADIATION DIFFUSION IN ATOMIC VAPOR IMAGING 48

Introduction 48
Experimental Setup 50
Results 54
Number density effects 54
Signal (λ_1) and pump (λ_2) laser effects 59
Conclusion 59

6 DETECTION OF SINGLE PHOTOELECTRONS IN A RESONANCE FLUORESCENCE IMAGING MONOCHROMATOR 61

Introduction 61
Experimental Setup 62
Results 63
Spatial distribution of single photoelectrons 63
Amplification effects on single photoelectron Detection 67
Conclusion 68

7 DETECTION OF MIE SCATTER USING A RESONANCE FLUORESCENCE DETECTOR 71

Introduction 71
Experimental Setup 72
Results 77
Conclusion.. 78

8 FINAL COMMENTS 79

Conclusion 79
Future Work 82

REFERENCES 85

BIOGRAPHICAL SKETCH 90

Abstract of Dissertation Presented to the Graduate School
of the University of Florida in Partial Fulfillment of the
Requirements for the Degree of Doctor of Philosophy

A RESONANCE FLUORESCENCE MONOCHROMATOR FOR SPECTRALLY-SELECTIVE IMAGING

By

Dimitri Pappas

January 2002

Chairperson: James D. Winefordner
Major Department: Chemistry

The main goal of the work described in this dissertation was to develop a novel imaging detector based on the absorption of light and subsequent fluorescence by an atomic vapor. This detector, a resonance fluorescence imaging monochromator (RFIM), has a spectral resolution and instrument response that is governed by the properties of the atomic vapor used as the sensing element. The RFIM operates by absorbing signal light that coincides with the narrow absorption profile of the atomic vapor (typically <1 GHz). Atoms that absorb the resonance signal light are then excited to a higher energy level using a pump laser, and fluoresce to the ground state via a third transition. In this work, a RFIM using Cs was developed for near-infrared imaging.

The operating environment of the RFIM was studied with respect to collisional losses in the cell in order to determine the best conditions to obtain a large quantum efficiency. A two-dimensional imaging detector with a spatial resolution of 200 μm was

developed in order to demonstrate the two-dimensional imaging capabilities of the detector. The effect of radiation trapping on the spatial resolution was investigated, and the degree of radiation trapping in the cell was minimized in order to improve the spatial resolution.

The spectral response of the detector was found to be approximately 400 MHz, which was limited by the Doppler-broadened linewidth of a single hyperfine transition of the signal step (852.12 nm). The out of band rejection of the RFIM was large, and signals as little as 1 GHz from the center of the RFIM absorption frequency were attenuated to less than 1%.

The sensitivity of the RFIM was demonstrated by detecting single photoelectrons from the intensified charge-coupled device camera used to detect the output fluorescence from the imaging detector. Each photoelectron detected corresponded to 10^4 photons (2 femtowatts, 10^{-15} W, at 852.12 nm) per pixel, which was the ultimate limit of detection for the RFIM reported in this work. A Mie scattering spectrum from a suspension of particles was obtained in order to demonstrate the narrowband photon detecting capabilities of the RFIM.

CHAPTER 1
AN INTRODUCTION TO NARROWBAND IMAGING

Atomic vapors have been used in spectroscopic applications where high background rejection and spectral resolution are required. Conventional photodetectors, such as photodiodes, photomultiplier tubes (PMTs), and charge-coupled devices (CCDs), respond over a wide spectral range in the ultraviolet, visible, and near-infrared regions (approximately 200–1000 nm). This wide spectral range is useful for many applications, such as in the detection of several wavelengths of light (for example, the output of monochromators, color imaging cameras, etc.); however, there are several applications which require high spectral resolution and high background rejection, which cannot be delivered by these conventional photodetectors.

Applications that require high spectral resolution include laser Doppler velocimetry; Brillioun, Mie and Rayleigh scattering spectroscopy; Raman spectroscopy and imaging; and long-range free-space telecommunications. In these applications, photodetectors must be able to discriminate between small frequency differences on the order of 30 GHz (1 cm^{-1}), or less [1]. In order to use conventional imaging detectors, which are commercially available at low cost and are well characterized, an additional spectral filtration step must be used in order to obtain high spectral resolution. Spectral filters commonly used in imaging applications include acousto-optic tunable filters (AOTFs) [2], liquid-crystal tunable filters (LCTFs) [3], liquid-crystal Fabry-Perot interferometers (LCFPIs)[4], dual-grating filters [5], scanning line imaging

monochromators (SLIMs) [6], fiber-optic bundle arrays (coupled to grating spectrometers and CCD detectors) [7], and simple dielectric interference filters [8].

All of these wavelength selection devices have advantages and disadvantages that vary with each application. Acousto-optic filters, for example, exhibit a high transmission efficiency (40-50%), but have a relatively large spectral bandpass on the order of 50 cm^{-1}. This bandpass is suitable for molecular luminescence imaging, but this filter cannot be used for high spectral resolution imaging applications. Acousto-optic filters also suffer from imaging distortion due to dispersion of the AOTF crystal within the bandpass of the detector. Liquid crystal filters have smaller bandpasses on the order of 10 cm^{-1} for both filters, but the transmission efficiency is low (15-25% for both types of filters). Liquid crystal filters offer fast wavelength scanning or switching–i.e. changing wavelengths directly without scanning–but the operation of such filters can be complex as more than one filter stage is necessary. Dual-grating filters, which use two parallel, holographic transmission gratings to isolate images according to wavelength, have large bandpasses (200 cm^{-1}) and a high transmission efficiency (75%). The large bandpasses, and the fact that the filter is subject to severe imaging blurring with the slightest misalignment of the gratings, make this filter a poor choice for spectroscopic imaging. Scanning line imaging monochromators have bandpasses limited by the spectrometer used (typically 1-10 cm^{-1}), and generate line-scanned images which require a long analysis time because only a portion of the image–a single line in one dimension–is acquired during a given integration time. Fiber bundle arrays have spectral characteristics governed by the type of spectrometer used, and offer the possibility for remote image detection; however, the spatial resolution is limited by the diameter of the

fiber, and current fiber imaging quality is typically worse than other imaging filters used in spectroscopic applications.

All of the previously mentioned imaging filters suffer from a trade-off between spectral bandpass and throughput, as well as image degradation. While some of the filters mentioned can achieve a spectral resolution on the order of 1 cm^{-1}, none approach the GHz or MHz level (3 x 10^{-2}–3 x 10^{-5} cm^{-1}), which is required for ultrahigh resolution photon detection and imaging. It should be noted that while optical heterodyne detectors can achieve ultrahigh spectral resolution, the optical throughput of a heterodyne detector or array of such detectors is very low, making imaging difficult. One device, the resonance fluorescence imaging monochromator, promises high sensitivity without sacrificing resolution, and can produce images comparable in quality to standard imaging systems. Based on the selective absorption of resonance light, subsequent excitation of the atoms absorbing the resonance light, and fluorescence of those atoms to the ground state *via* a second resonance transition, the resonance fluorescence imaging monochromator (RFIM) has a spectral bandwidth limited primarily by the absorption linewidth of the atomic vapor used. Figure 1-1 depicts the operation of the resonance fluorescence imaging monochromator. Photons whose frequency falls within the narrow linewidth of the atomic vapor (Cs in this case) are imaged with a lens into the front of the vapor cell and are absorbed by atoms in the atomic vapor. These excited items are then further excited to a higher excited state by a laser beam tuned to the pump transition, λ_2. This pump beam is transformed into a sheet of light as it enters the cell and forms the image plane just behind the input window. The image plane is analogous to a CCD image plane or a sheet of photographic film. The sequentially-excited atoms then

radiatively decay to the fluorescence level. The excited atoms then emit a second photon, the detection wavelength λ_f, to relax to the ground state. This λ_f fluorescence is collected by a dichroic mirror and imaged onto a CCD or other imaging device to form the final RFIM image. In this way, images can be obtained with high spectral resolution, limited by the linewidth of the atomic vapor used in the RFIM.

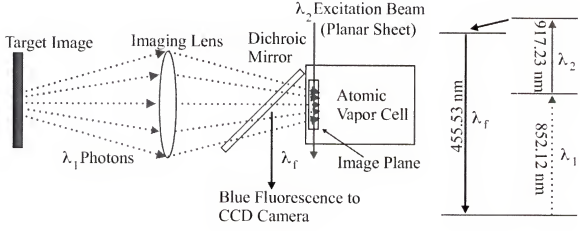

Figure 1-1. Schematic of the RFIM function and relevant energy levels involved in the two-step excitation/fluorescence scheme.

The goals of this work were to develop an atomic imaging filter based on cesium vapor in order to obtain images with high spatial resolution, high spectral resolution, and high sensitivity. In order to design an efficient RFIM, the spectroscopy of Cs must be well understood. Cesium was chosen as the active element in the RFIM because of its high vapor pressure at room temperature, the fact that it is monoisotopic (it should be noted that while Cs has more isotopes than any other element, all but ^{133}Cs are fission products, and only the main isotope is found in solid cesium metal), and for the large oscillator strength, f_{ij}, of the ground state resonance transition (852.12 nm, $f_{ij} = 0.72$).

The transitions used in the excitation scheme occur in the near infrared (852.12 nm and 917.23 nm for the signal (λ_1) and pump (λ_2) transitions, respectively). This wavelength region can be reached using conventional diode lasers, making the instrumentation for this detector relatively simple and robust in comparison with narrow-linewidth, pulsed tunable laser systems. This wavelength region is also useful in the fields of biology and biochemistry as near-infrared light can penetrate through tissues and cells effectively, with minimal photodegradation.

The design of the Cs RFIM centered on the understanding of the spectroscopy involved in the excitation scheme. Early studies in this work focused on the investigation of collisional excitation and ionization in dense Cs vapor. These studies helped to elucidate the optimum environment for the Cs atoms in the RFIM, and to understand the collisional processes that can cause nonselective excitation and ultimately reduce the efficiency of the detector. The collisional mixing due to the presence of buffer gases, as well as any trace gas impurities, was also studied. The level mixing was modeled using the density matrix formalism, and verified experimentally. Once the optimum conditions for the Cs vapor were understood, a suitable excitation scheme was chosen and used to detect photons through the excitation and subsequent fluorescence of the Cs vapor.

The Cs RFIM was further studied with respect to quantum efficiency, spatial and spectral resolution, and other spectroscopic parameters such as the degree of radiation trapping in the cell and its effect on the system performance. The minimum detectable number of photons was determined, and single photoelectrons were detected from a faint (2 fW) signal at 852.12 nm. The final studies in this work demonstrated the ability of the

RFIM to detect narrowband signals from scattering samples. To this end, the Cs RFIM was designed and evaluated for narrowband imaging.

CHAPTER 2
COLLISIONAL EXCITATION/IONIZATION IN CESIUM VAPOR

Introduction

Irradiation of a gaseous sample with a laser can induce a plasma *via* several processes. Dielectric breakdown in a gas is typically accomplished by using high irradiance lasers (approximately in the GW/cm^2 range) [9]. Although the threshold for plasma formation varies with many parameters, such as wavelength, gas composition and pressure, in general, these plasmas are formed through several non-resonant mechanisms such as multi-photon ionization and inverse *bremsstrahlung*. Inertial confinement plasmas are generated in this manner using several lasers with high irradiances. At sub-threshold laser irradiances (MW/cm^2), a resonance absorption step must first occur, populating an excited state of an atomic vapor. This effect, named laser ionization based on resonance saturation (LIBORS), requires that the excitation laser is tuned to an atomic transition of a major component of the vapor [10]. The formation of a plasma under these conditions occurs via superelastic collisions between seed electrons formed by resonant excitation and collisional ionization and excited-state atoms in the vapor. The superelastic collisions cause energy transfer between the excited-state atoms and the electrons, creating an avalanche effect that results in the ionization of the atomic vapor. While the laser irradiance in this case is lower, pulsed lasers of high energy are still required in order to observe plasma formation.

The plasmas mentioned above are all generated using pulsed lasers with high peak powers. In this study, the formation of a plasma formed by a relatively low irradiance continuous wave laser was investigated in order to understand the collisional ionization processes in Cs vapor filters used for photon detection. A heated Cs vapor cell was used to produce a highly ionized plasma when a continuous-wave (cw) Ti:Sapphire laser was tuned to the 852.12 nm ($6^2S_{1/2} \rightarrow 6^2P^o_{3/2}$) resonance transition of Cs. The large oscillator strength of this Cs transition, coupled with the relatively narrow laser linewidth (2 GHz), provides an environment in which the laser radiation is completely absorbed by the optically thick Cs vapor.

The collisional ionization and plasma formation processes can decrease the quantum efficiency in an atomic vapor filter by depopulating the first excited state of the atomic vapor. To this end, the plasma formation in dense Cs vapor was studied.

Experimental Setup

The experimental setup is shown in Figure 2-1. A single-mode, tunable, continuous-wave Ti:Sapphire laser (Schwartz Electro-Optics, Inc., Orlando FL) is pumped by the all-lines output of an argon-ion laser (Model 2060, Spectra-Physics, Mountainview, CA). The Ti:Sapphire laser was operated in standing wave mode, with a power output of 75–150 mW and a linewidth of approximately 2 GHz (0.005 nm at 852.12 nm). The beam from the laser was directed through a variable neutral density filter operated by a stepper motor. Using this filter, the laser intensity could be adjusted to the desired irradiance. The beam then passed through a Cs vapor cell made from a modified Cs spectral lamp. The outer envelope of the lamp was cut open in order to gain access to the lamp electrodes. The lamp ignition resistors were removed and the

electrodes of the lamp were used without further alteration (Figure 2-2). The lamp contained metallic Cs as well as a buffer gas (Ar in this case). In order to obtain a suitable number density of Cs atoms, the lamp was heated by wrapping a portion of the

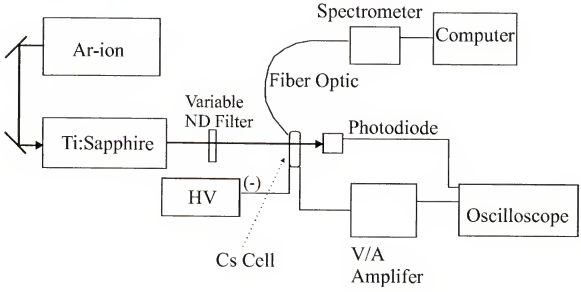

Figure 2-1. Experimental setup of the plasma system.

outer glass envelope with heating tape. The temperature in the lamp was controlled by varying the AC voltage on the heating tape. A thermocouple placed between the glass envelope and the inner Cs cell gave an approximate temperature of the cell once equilibrium was reached. The Cs vapor pressure in the cell can be calculated using the following [11]:

$$\log P = 5.006 + 4.165 - 3830/T \qquad (2\text{-}1)$$

where P is the vapor pressure in Pascals and T is the temperature in K. This formula is only valid for T between the melting point (301 K) and boiling point (944 K) of Cs. At the temperatures used in our experiment, the number density varied from 10^{12}–10^{13} atoms/cm^3. At these number densities the Cs vapor behaves as an optically thick medium

for the 852.12 nm beam. In addition to the Cs lamp, a second sealed Cs cell was also used for some measurements. This cell was made of borosilicate (Pyrex) glass and contained Cs under a vacuum. This cell was used without any modifications and was heated in a similar manner as the first cell.

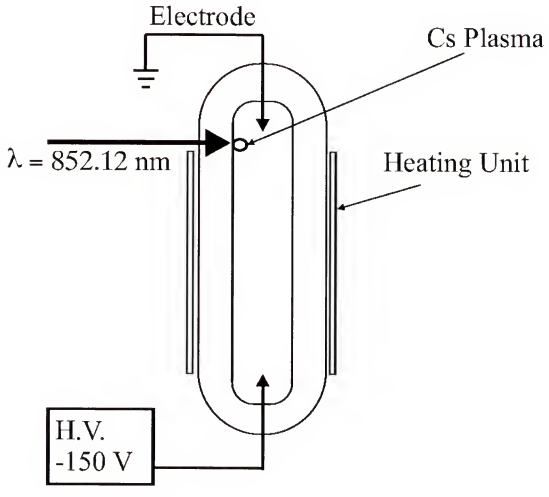

Figure 2-2. Schematic of the plasma cell.

The emission from the plasma was collected *via* a fiber optic cable and transmitted to a dual channel compact spectrometer (Ocean Optics, SD2000). The first spectrometer channel had a spectral window of 300 nm to 900 nm, and a resolution of 6 nm. A second spectrometer channel with a 1 nm spectral resolution and a spectral window of 210 nm to 875 nm (Ocean Optics SD2000, Dunedin, FL USA) was also used for higher resolution. In order to obtain ionization information, the electrical signal from the plasma was also recorded. The cell was illuminated near one of the electrodes inside the lamp, and a voltage of -12 to -120 VDC was applied to the opposite electrode. The electrical signal passed through a current-to-voltage amplifier (Keithley Instruments) and was recorded on an oscilloscope (Tektronix 5000A). Both optical and electrical signals were obtained simultaneously, although it should be stressed that the plasma formation was independent of the presence of any electric field. The plasma emission was intense and was visible to the eye.

In addition to the Ti:Sapphire laser, a diode laser operating near 852 nm was also investigated. The diode delivered 1-5 mW of multimode radiation to the cell. Course tuning of the diode was achieved by cooling the diode and the current was adjusted slightly to tune the diode laser into resonance with the Cs absorption line. The diode laser was driven by a battery-powered diode laser current source (ILX Lightwave, Model LDX 3620) and cooled with a thermoelectric cooling element adjusted by a temperature controller (ILX Lightwave, Model LDT5910). The typical power from the diode laser was between 1.0 and 2.5 mW.

For the Cs dimer absorption experiments, the attenuation of a helium-neon laser beam at 632.8 nm was used. The laser beam passed through the heated Cs cell and then through an interference filter (630 nm, 10 nm bandpass). The light was then detected

with a photomultiplier tube (Hammamatsu R1547) and the signal was measured using a strip chart recorder (Fischer Scientific). The incident intensity, I_0, was taken as the intensity of the laser as it passed through the Cs cell at room temperature. A 0.3 neutral density filter was used in order to assure the linearity of the detector.

Results and Discussion

Cs dimer measurements. One possible mechanism for the formation of a plasma is the ionization of Cs dimers. Cs dimers have been shown to be easily ionized with an absorption spectrum that spans the near infrared region [12]. It is unlikely that the plasma formation is due to the excitation and ionization of Cs dimers, because the plasma is wavelength dependent and extinguishes when the laser is tuned off resonance of the 852.12 nm line. The narrow-band wavelength response of the plasma ignition process indicates that the mechanism proceeds via an atomic transition. However, in order to verify this hypothesis, the presence of Cs dimers had to be confirmed. By measuring the optical absorption of Cs_2 the number density of the metal dimer can be determined. The Cs_2 number density is also important as high dimer concentrations can cause spectral interferences when operating a Cs resonance fluorescence monochromator, because Cs_2 absorption bands span the visible and near infrared spectrum. Cesium dimers can undergo photolysis after absorbing a photon and create two excited $6^2P^o_{3/2}$ atoms. In a resonance fluorescence detector, this can cause a false signal over a wide range of wavelengths. A large absorption band near 630 nm was chosen for this study as the band is easily probed with a simple helium-neon laser.

The transmittance of the laser beam through the cell was measured as a function of temperature by heating the cell. No absorbance was measured up to the temperatures used in this study (350 K). These results agree with those found by Sarkisyan *et al.* [13]. Due to the fact that the Cs_2 number density was very low, ($<10^8$ cm^{-3}) we conclude that the formation of the bright, highly ionized plasma does not involve the dissociation Cs_2.

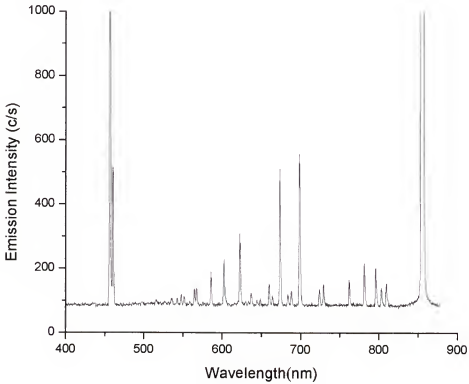

Figure 2-3. Emission spectrum of the Cs plasma.

Emission of the Cs plasma. In order to understand the mechanism of plasma formation, and to verify that Cs was the only element excited in the plasma, the emission spectrum was recorded. Figure 2-3 shows the doublet emission from the 7^2P states as well as several highly excited states (see Figure 2-4 for the energy level diagram corresponding to the plasma emission lines) such as the 7^2D, 8^2D, and 9^2D states.

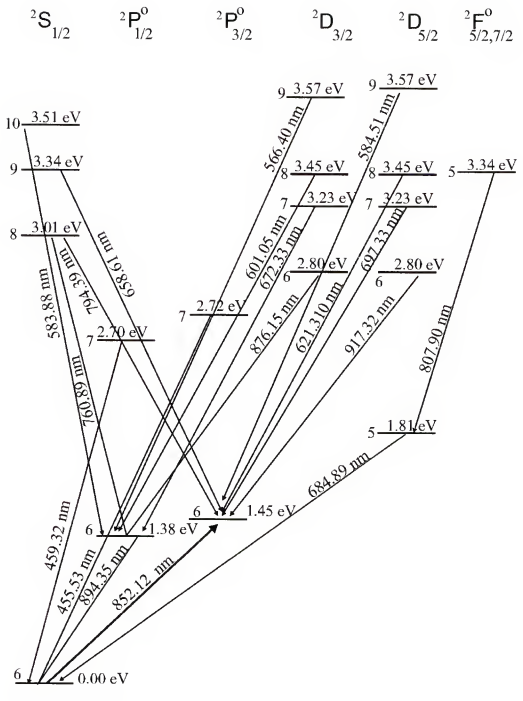

Figure 2-4. Partial energy level diagram of Cs showing the transitions observed in the plasma. The energy level spacing is not to scale. Adapted from reference 33.

Emission from these and other high-lying excited states–states 2 or more eV above the energy level of the $6^2P^o_{3/2}$ state–suggest that the emission is due to the recombination of electrons and ions. The weaker emission lines of the 72P doublet are observed when illuminated with the diode laser; the emission intensity is two orders of magnitude lower.

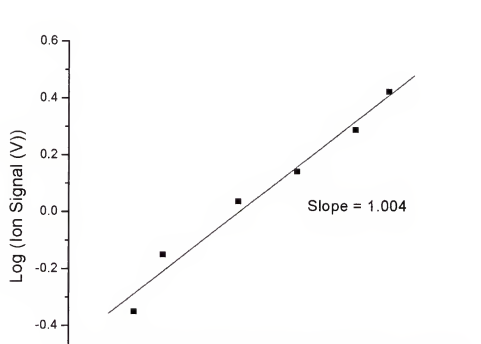

Figure 2-5. Log-log plot of the current measured in the plasma as a function of laser power.

While an intense plasma is not observed in this case, collisional excitation is still prevalent, generating blue fluorescence (455.53 nm and 459.95 nm) without the presence of a second excitation step (λ_2). This single-step pumping scheme, followed by collisional excitation, is not as selective as a two-step excitation scheme because

excitation at 894.35 nm produces similar, indistinguishable signals. The smallest Ti:Sapphire laser power observed to form a plasma using optical detection was 200 μW. The diode laser power was also estimated to be < 500 μW as the 2 mW laser beam was distributed over several intense modes, with only one mode absorbed by the Cs vapor. This is also observed in optical absorption measurements of the diode, where the peak absorption was typically 20% of the total incident light.

Current in the Cs plasma. Electrical current was measured in order to determine the degree of ionization in the plasma. In addition, the current generated in the plasma was measured as a function of laser intensity in order to ascertain whether or not the plasma was generated by a multi-photon process. A log-scale plot of current signal as a

function of laser intensity is shown in Figure 2-5. The slope of the log-log plot is 1.004, indicating that the mechanism is due to single-photon excitation. This is a reasonable observation because the low laser powers that were used make a multi-photon event unlikely.

The current generated in the plasma was also used as an indication of the ionization efficiency of the system. The ionization efficiency is typically defined as the number of ions formed per atomic excitation [14]. The number of atomic transitions that occur in a given time period for a cw laser is given by the number of photons that are absorbed. This approximation is valid in this case as the medium is optically thick and the rate of diffusion of atoms into the laser irradiation volume is equal to the ion depletion rate. The relative rates of diffusion and depletion can be observed by modulating the laser intensity and observing the square-wave ion current. If the signal is truly square-wave, then the conditions in the plasma are steady state. If there is decay of the signal, however, the approximation will not be valid. In our measurements the atom

diffusion rate into the cell was equal to the ion depletion rate, and the absorbance of the medium yielded the number of atomic excitations in a given time period. The absorbance

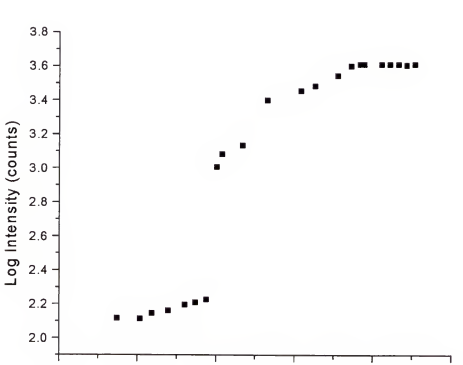

Figure 2-6. Emission Intensity of the $8^2D_J \rightarrow 6^2P^o_{3/2}$ doublet as a function of cesium number density. The transition point at approximately 10^{12} cm^{-3} indicates the threshold number density required for the multi-bodied collision that causes ionization.

measurements when the cell was heated to its highest number density (10^{13} atoms/cm^3) was too large to measure accurately, so the cell temperature was reduced. The temperature was lowered to 310 K where the atomic number density was $.10^{11}$ cm^{-3}. The

absorbance measured at this temperature was 0.766, which corresponds to 10^{17} photons absorbed at the laser power used. The number of electrons measured in the same 1 s time period was 10^{14}. The number of ions formed per atomic excitation was therefore 0.001.

The smallest laser power that could be detected by measuring the electrical current of the plasma was 4 μW. This measurement was limited by the large amount of background noise generated by the current-to-voltage amplifier. The ionization efficiency measured gives an estimate of the approximate loss in the atomic vapor filter operated at high temperature.

Effect of the Number Density of Cs Atoms. The Cs plasma increased in optical and electrical intensity linearly with the laser irradiance. When the cell was heated from room temperature up to the operating temperature of 370 K, the emission from the plasma is observed to intermittently ignite and extinguish and the linear plasma dimension (length along the laser axis) is observed to shorten and finally collapse to less than 1 mm from the glass. This intermittent formation of the plasma continues until the frequency of these sparks increases and the plasma finally ignites into a steady state plasma. A plot of optical intensity *vs.* number density is shown in Figure 2-6. Faint emission from the 7^2P and 6^2P states are observed at lower temperatures but intense plasma emission does not occur until the temperature of the cell reaches 350 K. The actual temperature of the cell could not be measured, however, and the temperatures measured with the thermocouple reflect a temperature that is undoubtedly slightly higher than the temperature within the inner envelope of the cell. The nonlinearity of the plasma emission with respect to number density of Cs atoms suggests that the plasma formation process is collisionally initiated.

The collisional cross section of excited Cs atoms with ground state Cs atoms is large (typically 100-1000 times) compared to the cross section for a Cs atom colliding with a buffer gas [15]. In an optically thick medium where the atoms are being pumped through a strong transition, the probability for energy transfer between colliding atoms is high. This mechanism of energy transfer is a possible mechanism for the formation of the Cs plasma. In order to test this hypothesis, two sealed Cs cells filled with 500 torr and 150 torr of nitrogen gas were used as well. When heated to the same temperatures, and up to a maximum temperature of 450 K, no plasma emission or electrical signals were observed. This is likely explained by the effective quenching of nitrogen, depopulating the excited $6^2P^o_{3/2}$ state.

Conclusion

The formation of a highly ionized Cs plasma using a relatively low power laser to excite a resonance transition was observed. The irradiance of the Ti:Sapphire laser was on the order of 1.5 W/cm^2, which is significantly lower than the irradiances used in conventional laser-coupled plasmas (MW/cm^2–GW/cm^2). The mechanism for the formation of this plasma is still unknown, however several clues to its origin have been reported. The linear dependence of laser power and irradiance on the emission and electrical signals indicates that a one-photon process is responsible for the plasma formation. The nonlinear dependence of the intensity of the emission from the plasma on number density indicates the plasma is formed by a collisional process. The plasma formation can cause a decrease in the quantum efficiency of a resonance fluorescence detector by depopulating the $6^2P^o_{3/2}$ state *via* a collisional excitation/ionization step. In

other to avoid collisional losses, the number density of the cesium atoms in the cell must be lowered to the 10^{11}–10^{12} atoms/cm^3 range . This will minimize collisional losses while maintaining an optically thick medium in the vapor cell.

CHAPTER 3
FLUORESCENCE MONITORING OF LASER-INDUCED POPULATIONS CHANGES IN CESIUM VAPOR

Introduction.

While the collisional losses that result in ionization were investigated, lower temperature cells were still prone to collisional mixing by buffer gases and trace impurities. Fluorescence dip spectroscopy is a useful technique in atomic fluorescence and resonance ionization spectroscopy for investigating optically and collisionally induced level population losses. The measurement of the population depletion of an energy level *via* resonance excitation to a higher state provides insight into the mechanism of multi–level excitation of atomic vapors [16-18]. The fluorescence dip technique has been applied to the investigation of autoionization cross–sections of atoms in flames [19], as well as to the measurement of the quantum efficiency of atomic fluorescence [20]. The change in the populations of the atomic energy levels provides insight into the various processes that occur during multi–photon excitation, such as fluorescence and quenching effects. Early work in fluorescence dip spectroscopy focused on the rovibronic spectroscopy of benzene [21] and nitrous oxide [22-23] in supersonic jets, while later studies reported the use of fluorescence dip in the study of atomic vapors [24] and the mechanisms of atomic fluorescence.

In previous work on Cs vapor, fluorescence dip spectroscopy was used to observe pulsed and continuous wave (cw) excitation to measure ionization efficiencies of direct photoionization of excited P and D states [25,26]. These studies observed a fluorescence

dip indicating a depletion of the excited state population due to photoionization. From these fluorescence dips, the cross–section of photoionization and the ionization efficiency, were measured. The fluorescence dips typically observed in atomic vapors are due to the depletion of an excited state. Using the density matrix formalism, Ljungberg [27] predicted that an enhancement in the population of an excited state could also occur in the multi–step excitation of atomic vapors. The enhancement of fluorescence intensity results from an *increase* in the population of the excited level by de-excitation of a high–lying excited state to the fluorescing level. This fluorescence enhancement was first observed by Simeonsson *et al.* [28] and was modeled using the steady–state rate equation approach.

In the investigation of using cesium vapor as an efficient resonance fluorescence monochromator, fluorescence dip spectroscopy was used to monitor collisional mixing of 6P and 6D levels. The excitation scheme studied is the double–resonance cw excitation to the $6^2D_{5/2}$ level from the $6^2P^o_{3/2}$ level, followed by cascade fluorescence to the $7^2P^o_{3/2}$ level and then to the ground state. By monitoring the fluorescence signals from both P and D levels, induced by one– and two–step laser excitation, several interesting observations were made, indicating the important role played by the collisional mixing between the various levels. The aim of this chapter is to report the observed reduction and enhancement of the fluorescence signals observed, to evaluate how these depletion effects change the efficiency of the resonance fluorescence detector, and to compare the observed signals with those which can be predicted by a simplified excitation formalism approaching the experimental conditions.

Experimental Setup

The experimental setup is shown in Figure 3-1. A single–mode, tunable, continuous–wave Ti:Sapphire laser (Schwartz Electro–Optics, Inc., Orlando, FL) is pumped by the all–lines output of an argon–ion laser (Model 2060, Spectra Physics, Mountainview, CA). The Ti:Sapphire laser was operated in standing wave mode, with a power output of 100 mW and a linewidth of 2.6 GHz at 917.23 nm. The Ti:Sapphire laser is used to excite atoms from the excited $6^2P^o_{3/2}$ state to the $6^2D_{5/2}$ state (see Figure 3-2 for a partial energy level diagram of Cs). For the first transition in our excitation scheme, a diode laser operating at 852.12 nm was used. The diode delivered 1–5 mW of multimode radiation to the Cs cell. The linewidth of each mode should be approximately 100 MHZ, however the effective linewidth of the laser is much larger due to the presence of several modes with approximately the same intensity. Course tuning of the diode was accomplished by cooling the laser, and the current was adjusted to achieve fine tuning in order to reach the peak of the Cs absorption line. The diode laser was driven by a battery–powered diode laser current source (ILX Lightwave, Model LDX 3620) and cooled with a thermoelectric cooling element adjusted by a temperature controller (ILX Lightwave, Model 5910). Typical power from the diode was approximately 1 mW, as the current used to reach the absorption line was near the lasing threshold current.

The two laser beams intersected in a sealed pyrex cell containing metallic Cs and Ar buffer gas. Both lasers had a beam diameter of approximately 1 mm. Two high–pressure cells were used (see below), however the experimental conditions were kept the same for each cell. In order to obtain a suitable absorption of resonant photons, each cell was heated to produce a high number density of Cs atoms. One cell was 1 cm

long and 2.5 cm in diameter (Opthos Instruments, Rockville, MD, USA), and the second was a modified Cs spectral lamp (Osram, Oriel Instruments, Stratford, CT, USA). The Cs lamp consisted of an inner cell containing Cs and two electrodes which was surrounded by a second cell that provided thermal and mechanical stability. The length of the cell containing Cs was 6 cm and the width was 1.5 cm. The outer envelope was

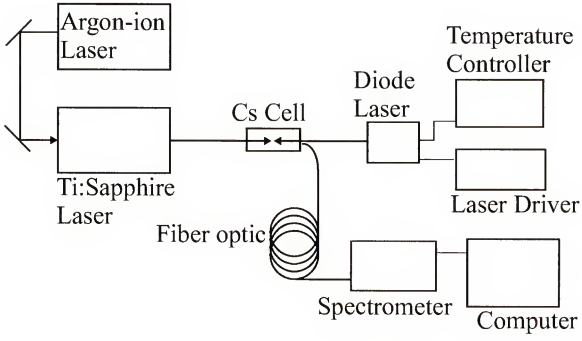

Figure 3-1. Experimental setup for the fluorescence dip experiments.

cut along the base in order to fill the space between the envelopes with air; this was done in order to ensure thermal conduction. The second cell was later used in order to measure electrical current (see below).

Cell temperatures varied between 45°C–50°C, providing a number density on the order of 10^{11} cm^{-3}. Cs–Ar collisions are expected to be important at these temperatures and number densities. These collisions are expected to mix n^2L_J levels in Cs, causing a

depletion of the excitation levels used in the resonance fluorescence detector. A thermocouple was used to measure the temperature outside of the cell, and each cell was heated for several hours before use in order to achieve thermal equilibrium.

Collisions might not only be efficient in level mixing, but also in ionizing excited atoms, further depleting the levels used in the RFD pumping scheme. In order to observe any ionization that might occur, the cell containing Cs and two electrodes (modified from an Osram lamp) filled with argon was used to measure electrical current. The cell was heated in a similar fashion and illuminated by the same two lasers. A –120 V potential was placed on one electrode, while the other was coupled to a current–to–voltage amplifier (Keithley Instruments); the output signal was recorded on a fast digitizing oscilloscope (Tektronics, Model 5000A).

Fluorescence from the Cs vapor was collected using a fiber optic cable and transmitted to a dual–channel compact spectrometer equipped with a linear CCD array (Ocean Optics, SD2000). The spectrometer had a spectral window from 300 nm to 900 nm, and a resolution of 6 nm. The fiber optic was placed adjacent to one of the cell windows at a point near where the diode laser beam entered the cell. The position of the fiber was such that the coupling lens (F/2) observed the fluorescence along the path of the laser beams. This near 180^{o} observation angle was used to ensure that the maximum amount of fluorescence was collected, and to eliminate any spatial effects when measuring fluorescence. Fluorescence was measured at the resonance line of Cs, 852.12 nm, as well as at 894.35 nm, which resulted from the collisional mixing between the $6^2P^o_{3/2}$ state and the $6^2P^o_{1/2}$ state. In addition, the 876.14 nm line due to fluorescence

from the $6^2D_{3/2}$ state (due to mixing of the $6^2D_{5/2}$ and $6^2D_{3/2}$ states) was also monitored (See Figure 3-2).

Modeling Simulations

Density matrix formalism. Because of the availability of a DensMat software package [29], it was felt interesting to apply this approach to the experiment. This software models the atomic level populations *versus* time in a two–step excitation

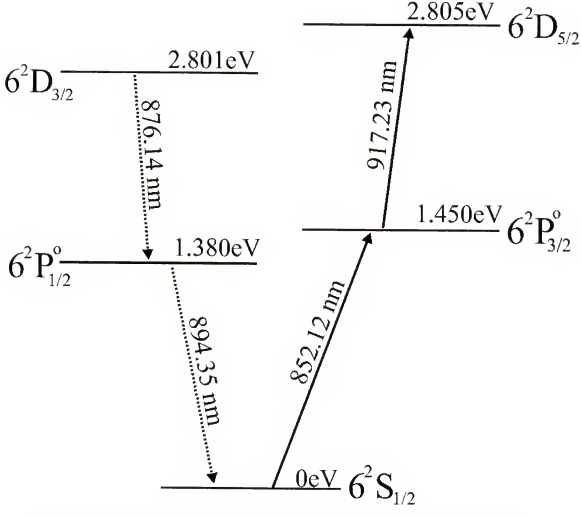

Figure 3-2. Partial energy level diagram of the transitions investigated. The energy levels of each level (eV) is shown.

experiment. The level populations can also be modeled using the steady–state rate equation approach, as described by Voigtman [30]. The key difference between the two models is that the density matrix approach considers coherent effects due to the high peak power of pulsed lasers. In the case of low–power cw lasers, coherent effects are not observed and either the density matrix or rate equation approach can be used to model the

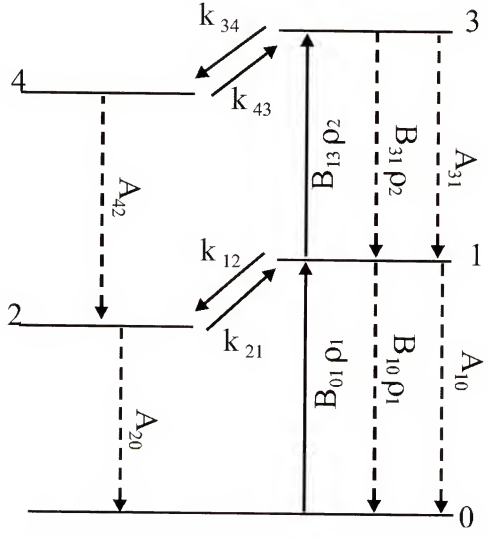

Figure 3-3. Partial energy level diagram of the transitions investigated, showing all pertinent radiative and collisional transitions (see Table 3-1).

Table 3-1. Rate constants for the Cs transitions used in this study (see Figs. 3-2 and 3-3).

Rate	Symbol	Transition	Value (s^{-1})[a]
Pumping Rate	$B_{01}\rho$	$6^2S_{1/2} \rightarrow 6^2P^o_{3/2}$	2.34×10^8
	$B_{13}\rho$	$6^2P^o_{3/2} \rightarrow 6^2D_{5/2}$	3.26×10^9
Stimulated Emission	$B_{10}\rho$	$6^2P^o_{3/2} \rightarrow 6^2S_{1/2}$	1.17×10^8
	$B_{31}\rho$	$6^2D_{5/2} \rightarrow 6^2P^o_{3/2}$	2.17×10^8
Spontaneous Emission	A_{10}	$6^2P^o_{3/2} \rightarrow 6^2S_{1/2}$	3.70×10^7
	A_{31}	$6^2D_{5/2} \rightarrow 6^2P^o_{3/2}$	1.74×10^7
	A_{42}	$6^2D_{3/2} \rightarrow 6^2P^o_{1/2}$	1.96×10^7
	A_{20}	$6^2P^o_{1/2} \rightarrow 6^2S_{1/2}$	3.30×10^7
Collisional Mixing[b]	k_{12}	$6^2P^o_{3/2} \rightarrow 6^2P^o_{1/2}$	2.5×10^5
	k_{21}	$6^2P^o_{1/2} \rightarrow 6^2P^o_{3/2}$	1.8×10^5
	k_{34}	$6^2D_{5/2} \rightarrow 6^2D_{3/2}$	3.0×10^6
	k_{43}	$6^2D_{3/2} \rightarrow 6^2D_{5/2}$	2.5×10^6

a. A_{ki} values taken from Radzig and Smirnov [33]. See also [32] for details.
b. Obtained from this work.

energy levels. As said stated earlier, we chose the density matrix approach because the software was readily available. Because DensMat is configured for pulsed excitation, a cw case must be treated as a long pulse as described above. This approximation holds true if steady–state conditions are reached relatively quickly with respect to the duration of the fictitious laser pulse. In our simulations, the rectangular laser pulse was set to 10 ms, and the measurement time lasted for the entire pulse duration. The atomic levels under investigation all reached steady–state conditions within 100 ns, proving the suitability of the approach.

The rates of population and depletion of the excited states considered are shown in Figure 3-3. Collisional quenching of the fluorescence lines should be negligible since the cell is filled with argon. Level mixing, however, is possible because the energy difference between these levels is small. The calculated rate constants, pumping rates, and other parameters used in these simulations are listed in Table 3-1.

Another assumption made in our simulations was that there was no photoionization of the atoms in the $6^2D_{5/2}$ state, which would have required the use of a trap level in the DensMat software. It is assumed that there is no photoionization due to the residual 917.23 nm beam, as well as any ionization due to collisions in the cell. No electrical signal was detected in the cell containing electrodes, indicating that at the laser powers and temperatures used no appreciable ionization occurred in the cell. The lack of any ionization proves that the neglect of an ionization trap in our simulations is a valid assumption.

Hyperfine structure [21] of both the ground and excited levels was neglected. This is justified by the fact that the cell was used for the modeling experiments is filled

with supposed to contain argon at relatively high pressure (760 torr). Indeed, an absorption scan made with the Ti:Sapphire laser (2 GHz linewidth) across the 852.12 nm line in the cell resulted in a broad absorption linewidth of about 28 GHz, which is significantly broader than the hyperfine structure of the levels studied.

Simulation results. The collisional mixing rates, k_{12} and k_{21} for the 6^2P states were calculated by assuming a three–level system. This was achieved experimentally by removing the 917.23 nm beam from the cell. In this case, the atoms are excited by the 852.12 nm diode laser to the $6^2P^o_{3/2}$ state. The excited atoms fluoresce to the ground state as well as transfer to the $6^2P^o_{1/2}$ state. A 894.35 nm beam provided by the Ti:Sapphire laser (output power = 80 mW) was also used excite atoms to the $6^2P^o_{1/2}$ state to monitor the inverse transfer to the higher 6^2P level. In the latter case, fluorescence at 852.12 nm was observed, although it was lower in intensity despite the fact that the pumping rate at 894.35 nm was higher. DensMat software was used to calculate the level mixing rates for both excitation conditions, in order to ensure that the calculations were valid. It should be noted that the cascade fluorescence resulting in the blue resonance fluorescence at 455.53 nm is accounted for in this simulation as a "deactivation" with a value of $6x10^4$ s^{-1}, which is the rate-determining step of the cascade transitions (see Chapter 4). The fluorescence intensities, corrected for instrument response, spontaneous emission coefficients, and degeneracy, can be used to estimate the relative populations of these excited states. Since the pumping rate, stimulated emission rate, and spontaneous emission rate are either known or calculated, the mixing rates can be estimated. By calculating the mixing rates of the 6^2P states using the three–level system, the mixing rates for the 6^2D states can be determined.

The estimated and known transition rates are listed in Table 3-1. The mixing rates for the 6^2P states are smaller than the mixing rates for the 6^2D states, which is expected as the energy difference between these states (0.07 eV) is larger than the energy difference between the higher lying 6^2D states (0.004 eV). The rates are relatively slow (10^5 and 10^6 s^{-1}), but this is expected since the cell is relatively cool. The accuracy of these values cannot be assessed. The model predicts the simultaneous depletion of the $6^2P^o_{3/2}$ state and the enhancement of the $6^2P^o_{1/2}$ state, which has been experimentally verified (see Table 3-2).

Experimental Results: Fluorescence Behavior of the $6^2P^o_{3/2}$ and $6^2P^o_{1/2}$ States. When the diode laser wavelength is set at 852.12 nm, both resonance and nonresonance (stepwise) fluorescence can be observed from the collisionally mixed 6^2P_J levels when the cell was heated to approximately 45–50°C. At these temperatures, and corresponding Cs number densities, virtually all of the 852.12 nm photons were absorbed. The experimental arrangement, however, ensured that light from the entire path length of the two laser beams was collected. The intensity of the nonresonance fluorescence from the collisionally populated $6^2P^o_{1/2}$ state was found to be temperature dependent, with strong fluorescence first observed at approximately 40°C. At temperatures higher than 60°C, collisional ionization of the atoms in the $6^2D_{5/2}$ state was observed; therefore, the cells were kept well below this temperature. Upon irradiation of the excited atoms with the 917.23 nm beam, fluorescence at 876.14 nm appeared, and an increase in the 894.35 nm luorescence was observed. In addition to the enhancement of 894.35 nm fluorescence, a depletion of the excited $6^2P^o_{3/2}$ state was marked by a decrease in the 852.12 nm f fluorescence intensity.

Table 3-2. Experimentally measured population changes (fluorescence intensities) of the P and D levels in the presence and absence of the second excitation step (see Figure 3-2.

Wavelength (nm)	I_{off} (counts/s)[a]	I_{on} (counts/s)[b]
852.12	1976[c]	1935
894.35	20	96
917.23	0	140
876.14	0	20

a. I_{off} = The fluorescence intensity of the line in the absence of the 917.23 nm excitatation step.
b. I_{on} = The fluorescence intensity of the line in the absence of the 917.23 nm excitatation step.
c. The standard deviation is 3 counts/s for all measurements.

The measured intensities of the 852.12, 894.35, and 876.14 nm fluorescence are shown in Table 3-2. These values were used to evaluate the mixing rates in Section 3 and collected in Table 3-1.

Conclusion

A continuous–wave excitation scheme for Cs which exhibits both enhancement and reduction of fluorescence has been reported. The enhancement of the 894.35 nm fluorescence was due to the radiative decay from the collisionally coupled $6^2D_{3/2}$ state, indicating that level mixing was efficient in the Cs cells. The cw case is unique in that the low pumping rates do not allow for efficient photoionization, therefore steady–state is rapidly reached. The experiment was modeled using the density matrix formalism by approximating the cw case as a rectangular pulse lasting several microseconds. Since the steady–state condition is reached within 100 ns, the approximation holds true and the fluorescence behavior of Cs can be predicted. The simulations show that when the excited $6^2D_{5/2}$ atoms are allowed to collisionally relax to the $6^2D_{3/2}$ state, the atoms then radiatively decay to the $6^2P^o_{1/2}$ state, increasing the population of that level. The enhancement of the intensity of the 894.35 nm line observed when the second excitation step is present is evidence of this mechanism. By measuring fluorescence intensities and fitting the density matrix simulations to these measurements, the rates of collisional mixing can be determined.

The poor characterization of both the excitation lasers and the Cs cell do not allow an accurate evaluation of the mixing rates and collisional cross sections, as reported, for example in the case of other Cs transitions, by Sasso *et al.* [32]. However, the

simulations and experimental measurements indicate that there are several pathways in which excited atoms, which could contribute to the RFM signal, are lost. Care must be taken to minimize collisional mixing in Cs cells in order to maximize the efficiency of the detector. To accomplish this, cells containing Cs without a buffer gas will be used. It is important to note that even small traces of impurity gases will cause efficient level mixing. With the use of Cs cells without buffer gases, the linewidth of the atomic lines is expected to narrow due to the removal of collisional broadening sources. The Cs–Cs collisions in the cell are not expected to cause significant broadening, and the linewidth of the absorbing atoms will be limited by the Doppler linewidth of the vapor. With the optimization of the Cs cell environment, the two-step excitation scheme can be applied to the RFD to evaluate the system's performance.

CHAPTER 4
A CESIUM RESONANCE FLUORESCENCE IMAGING MONOCHROMATOR

Introduction

Atomic resonance fluorescence filters and fluorescence imaging filters have been used in spectroscopic applications where high spectral resolution is essential. These atomic filters, based upon the absorption of resonance radiation and subsequent fluorescence, serve as one- and two-dimensional detectors with spectral bandwidths determined only by the linewidth of the absorbing vapor. An attractive feature of resonance filters is an absorption linewidth in the GHz to MHz (Doppler-free) range. Atomic vapors have been used extensively as resonance monochromators for atomic emission, absorption, and fluorescence, and have been reviewed by Matveev [34] and shown experimentally by Krupa *et al.* [35], among others [36-39]. Atomic resonance monochromators have been used in molecular spectroscopy as well, serving, for example, as a detector for rotational Raman scatter [40].

Resonance fluorescence monochromators have also been used to detect two-dimensional images with high spectral and spatial resolution. Matveev *et al.* [41] have used two-step excitation of Hg vapor to produce two-dimensional resonance fluorescence images. This resonance fluorescence imaging monochromator (RFIM) was used to demonstrate the imaging capabilities of the resonance fluorescence technique. Several imaging detectors based on the resonance fluorescence or ionization of mercury vapor [42-44] have been developed. The Hg RFIM and resonance ionization imaging detector

(RIID) worked well at 253.7 nm (corresponding to the forbidden $6^1S_0 \rightarrow 6^3P^o_1$ transition of Hg); however, this wavelength is difficult to reach unless pulsed lasers are used. There is considerable interest in creating continuous-wave (cw) RFIMs and RIIDs for the detection of Raman and Rayleigh scatter, as well as high resolution Doppler imaging. Cesium was chosen as the active element for this work because of its high number density near room temperature and large oscillator strength of the first resonant transition (852.12 nm, in addition the resonance transition of Cs at 894.35 nm can also be used as the first excitation step, although the succeeding excitation steps will differ from those listed herein). Cesium is also a monoisotopic element; therefore, the absorption lines are not complicated by isotope splitting. A Cs atomic imaging filter has been described previously [45]; however, this filter involved a two-step excitation scheme that used a relatively weak transition ($6^2P^o_{3/2} \rightarrow 8^2S_{1/2}$) for the second excitation step. The study reported in [45] used the same fluorescence wavelength (455.53 nm) as in this work; however, the cell geometries and pumping scheme differed dramatically. The current work uses a cell in vacuum, thereby narrowing the overall linewidth of the detector and improving the spatial resolution. In addition, the second pumping step in this work (917.23 nm) has a large oscillator strength, so saturation–a condition necessary for efficient operation of the RFIM–can be achieved at low irradiances.

Because the transitions used to pump the Cs atoms are in the near-infrared region, which is accessible to cw tunable diode lasers, the RFIM system can be compact and portable, and have minimal power consumption. Moreover, the wavelength (852.12 nm) to be detected is useful for many biological applications, for example, where visible and ultraviolet photons are strongly absorbed such as Raman spectroscopy in human tissue.

The ultimate goal of this project is to design a cw RFIM capable of high-resolution imaging in the near-infrared region. To this end, a cesium-based cw RFIM has been developed.

Experimental Setup

Two cw lasers were used for the two-step excitation scheme (Figure 4-1). For the signal (λ_1) laser step ($6^2S_{1/2} \rightarrow 6^2P^o_{3/2}$), a tunable, external-cavity diode laser (ECDL) (Model 2010A, Newport Corp., USA) was used. The laser output was single mode and tunable over a range from 845-860 nm, with a maximum output power at 852.12 nm of 16 mW. The laser linewidth was on the order of 1-5 MHz. Coarse tuning of the diode was accomplished by scanning the tuning mirror with a stepper motor in the Littman-Metcalf cavity, and fine tuning to the maximum of the absorption line was accomplished by adjusting the voltage on a piezoelectric element located behind the tuning mirror. The external-cavity diode laser beam was collimated as it entered the cell. A second external cavity diode laser (Model TEC-500, Sacher Lasertechnik, Marburg, Germany) was used as the pump (λ_2) laser. This laser had a linewidth of 5 MHz and a maximum power of 33 mW. The narrow laser line ensured that only one of the $6^2P^o_{3/2}$ hyperfine components was excited to the $6^2D_{5/2}$ state. This beam was also collimated as it entered the cell from the side (Figure 4-2), and cylindrical lenses were used to shape the beam into a sheet of light 12 mm in height and 1 mm wide.

The second ECDL (λ_2) was tuned to the 917.23 nm ($6^2P^o_{3/2} \rightarrow 6^2D_{5/2}$) transition of cesium. Atoms excited to this 6D state decay to the $7^2P^o_{3/2}$ state where they

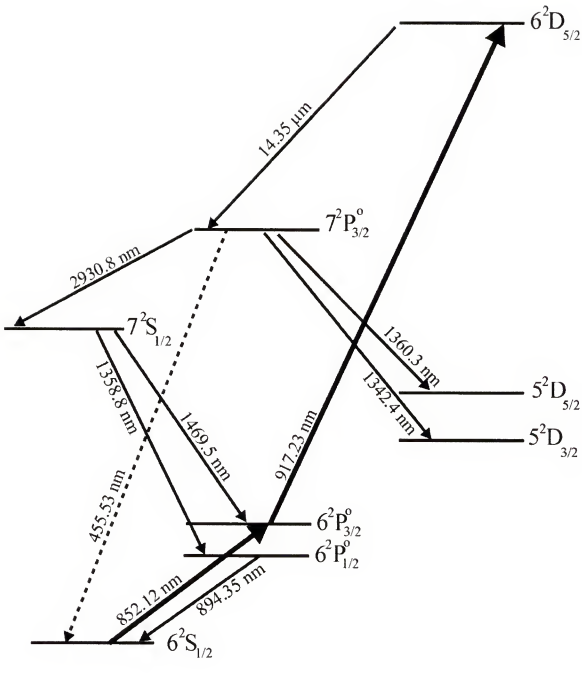

Figure 4-1. Partial energy level diagram of cesium, showing the atomic transition wavelengths used in the excitation scheme and the possible radiative losses in the RFIM. The energy level spacing is not to scale.

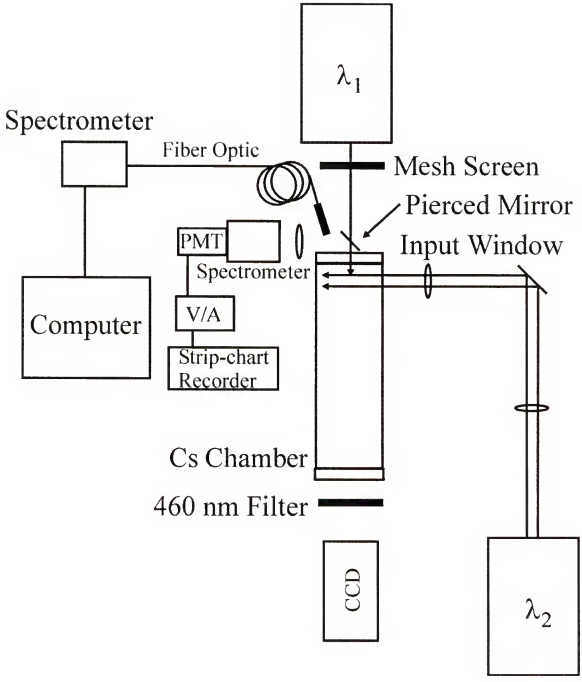

Figure 4-2. Experimental Setup of the RFIM

spontaneously emit (decay) to the ground state, emitting photons corresponding to the second resonance wavelength (455.53 nm) [46].

The cylindrical, Pyrex cesium cell used in this study (Opthos Instruments, Rockville, MD, USA) was 75 mm in length and had two windows 25 mm in diameter (see Figure 4-2), and contained Cs metal under a vacuum. A stainless-steel mesh screen was placed between the cell input window and the λ_1 laser. The mesh wires were 320 μm in diameter spaced at 1 mm intervals (this mesh served as the image source, the first excitation beam spot resembled the mesh as shown in Figure 4-3 for the imaging setup). A fiber optic placed close to the input window collected a small fraction of the laser scatter and the fluorescence. This collected light was passed into a compact spectrometer (Model USB2000, Ocean Optics, Dunedin, FL, USA, 750-950 nm spectral window), which served as a monitor of the laser wavelengths to verify that the lasers were tuned to the appropriate atomic transitions. A pierced mirror and lens near the cell collected a fraction of the fluorescence forming an image on the slit of a spectrometer (Model H-10, Spex Indust., Edison, N.J. USA). The light was then detected by a photomultiplier tube and amplified by a current-to-voltage amplifier, and read by a strip-chart recorder. The response of the monochromator and photomultiplier was calibrated using a standardized tungsten lamp. When both lasers were tuned to the appropriate atomic transitions, blue fluorescence was visible to the unaided eye.

The cell contained solid Cs metal under vacuum, which was heated slightly to control the number density of the Cs vapor between 10^{10} and 10^{12} cm^{-3}. The temperature was chosen (approximately 40-60 ^{o}C) to provide a sufficient number density of Cs, but was kept below 100^{o}C, at which point Cs-glass reactions were observed.. Fluorescence

images were captured by a digital CCD camera (Model Cybershot, DSC-S70, Sony, Japan) using an interference filter (7% transmission at 455 nm, 10 nm bandpass (FWHM)) and an 8 s integration time. The camera was connected to a computer *via* a universal serial bus (USB) cable. Images were further processed using the SigmaScan (SPSS, Inc. Chicago, IL, USA) software package.

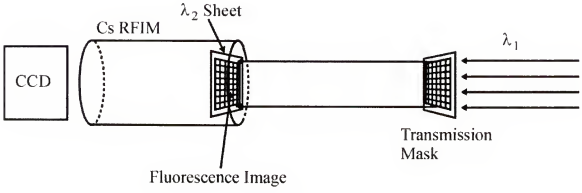

Figure 4-3. Schematic of the imaging experiment.

Results

Spectral response of the RFIM. Using the same system described in above, the frequency of the 852.12 nm (λ_1) laser beam was scanned by varying the voltage on the piezoelectric element in the external cavity. The resulting spectral response of the RFIM is shown in Figure 4-4. Both hyperfine components, separated by 9 GHz, can be seen in the response curve of the 852.12 nm fluorescence. The hyperfine components have a FWHM of approximately 0.4 GHz; however, only one hyperfine component contributes to the overall fluorescence signal at 455.53 nm, since the second ECDL has a sufficiently narrow linewidth to excite only one component. Therefore, the spectral response of the Cs RFIM is that of the Doppler-broadened linewidth of the excited hyperfine line, which

is approximately 0.4 GHz. As seen in Figure 4-4, the signal attenuation 1 GHz from the atomic line is on the order of 99%; it is evident that the RFIM can serve as an imaging detector with high background rejection and excellent spectral resolution. The detector can also be used to detect λ_2 photons if λ_1 is fixed at the desired resonance wavelength.

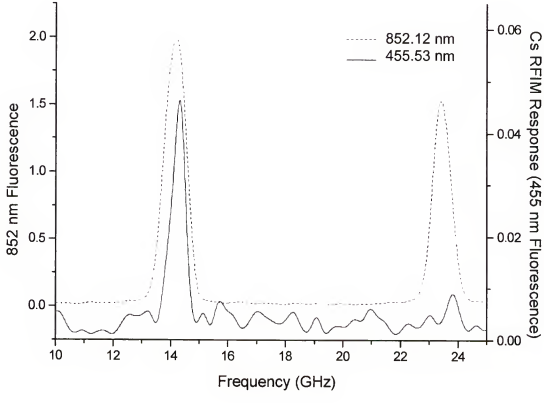

Figure 4-4. Spectral response of the RFIM to 852.12 nm photons.

Fluorescence intensity *vs.* photon flux. The power of the 852.12 nm laser was attenuated using neutral density filters in order to determine whether the fluorescence from the $7^2P^o_{3/2}$ state was linear with incident intensity. For these measurements, a pierced mirror (a flat mirror with a 45° angle hole drilled through the center) was used to collect the maximum amount of fluorescence from the cell, and a one-dimensional image

(the 852.12 nm laser beam without a mask) was used. The fluorescent light was detected by the photomultiplier tube. The plot of fluorescence signal as a function of photon flux at 852.12 nm is shown in figure 4-5. The log-log plot has a slope of unity typical for the linear behavior of this event. Measurement of the fluorescence signal as a function of the 917.23 nm laser light yielded similar results and the results are not shown. Taking the

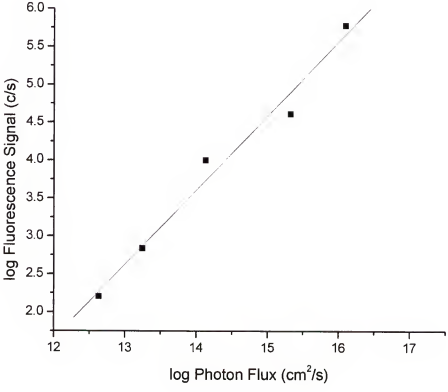

Figure 4-5. Fluorescence from the $7^2P^o_{3/2}$ state (455.53 nm) as a function of 852.12 nm photon flux. The slope of the line is unity.

limit of detection as $3\sigma/m$, where σ is the noise count in the blank (in this case, with the λ_1 lasers blocked), and m is the sensitivity (counts/photon s) of the detector, the limit of detection for this experiment was 10^{11} photons/s. The limiting factor in this experiment

was noise from the detector; incorporating a low-noise PMT into the system would greatly enhance the response of the RFIM.

Two-dimensional imaging with the Cs RFIM. Two-dimensional imaging is also an important feature of the RFIM. Figure 4-3 shows the schematic for obtaining an image. The beam from λ_2 enters the side of the cell and is shaped by lenses to form a sheet of light. The mesh-shaped λ_1 beam then interacts with the atoms inside the sheet of

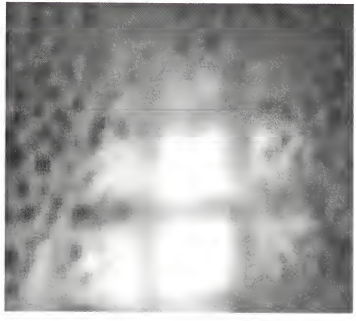

Figure 4-6. RFIM image of a stainless steel mesh (mesh bar diameter = 320 μm, interval = 1mm). The light areas indicate fluorescence.

λ_2 light producing fluorescence corresponding to the shape of the mask. The image from the 455.53 nm fluorescence is shown in figure 4-6. The fluorescence images due to two individual squares in the distortion-free area of the mesh are separated by a dark region of 320 μm. Despite this close distance, the dark space is clearly seen and the two squares (corresponding to the fluorescence signal) are resolved. Based on the separation of the

squares, the resolution is estimate to be on the order of 200 μm. The improvement in spatial resolution over other reported fluorescence imaging devices occurs because the atoms are in a vacuum in a relatively large cell, where collisions with foreign gas atoms do not occur and collisions with the walls of the cell are unlikely and do not cause significant image blurring.

Conclusion

The RFIM has been successfully used to obtain two-dimensional images with high spectral resolution. This technique is a compliment to resonance ionization imaging detection (RIID). The previous work with the Hg RFIM and RIID proved that while the spectral and spatial resolution of a detector can be the same, the quantum and collection efficiencies can differ. With an RIID, the quantum efficiency is expected to be the same or less than that of the RFIM; however, signal collection efficiency with the RIID can approach unity.

The fluorescence yield of the RFIM can be expressed as the number of fluorescence photons at the collection wavelength (455.53 nm) per atomic excitation, and is analogous to the quantum efficiency of the detector. The radiative pathways to other levels must also be considered (see Figure 4-1 for the all of the possible radiative pathways) when determining the fluorescence yield. The fluorescence yield or quantum efficiency is expressed as follows:

$$Y = \left(\frac{A_{14.35\mu m}}{A_{14.35\mu m} + A_{917.23nm}} \right) \cdot \left(\frac{A_{455.53nm}}{A_{455.53nm} + A_{2930.8nm} + A_{1360.3nm} + A_{1342.4nm}} \right), \qquad (4\text{-}1)$$

where A_λ is the spontaneous emission rate (Hz) of the transition of interest. This expression assumes that there is no significant quenching of the excited atoms, which is a

valid assumption for a low-pressure vapor cell. The maximum quantum efficiency is, therefore, the product of the branching factors from the highest excited level and the spontaneous emission level of interest. It is difficult to calculate a theoretical value for the fluorescence yield, as the saturation effects from the second laser step cause the behavior of the system to deviate slightly due to stimulated emission effects. The fluorescence yield from the $7^2P^o_{3/2}$ step can be calculated and is estimated to be 46%. The limiting step in the process, therefore, is the $6^2D_{5/2} \rightarrow 7^2P^o_{3/2}$ transition. For the pumping scheme used in this work, the measured fluorescence yield is 1 %, which is limited primarily by the $6^2D_{5/2} \rightarrow 7^2P^o_{3/2}$ rate constant. Taking the quantum efficiency of the CCD into account (50 % at 455.52 nm) and light collection efficiency of the lens and filter system (10% using low f-number lenses), the efficiency of the imaging device is about 0.05%. This sensitivity is on the order of that obtained using typical near-infrared photodetectors; however, the spectral resolution (400 MHz, or 9.7×10^{-4} nm at 852.2 nm) is several orders of magnitude higher than that of conventional photon detectors.

The RFIM has been demonstrated as a spectrally selective photon detector with spatial resolution on the order of 200 μm. The spatial resolution has also been improved because of the lack of collisions with foreign atoms, limiting the instrument response to the Doppler linewidth of one of the hyperfine absorption components of the 852.12 nm line. The current resolution of 200 μm can be improved by compromising between light collection efficiency and image preservation. Lower f-number lenses will increase light collection, however the edges of the image will be distorted in this case. The spectral resolution is limited by the Doppler-broadened linewidth of one of the hyperfine levels of the Cs ground state (0.4 GHz). Further studies of the RFIM operation include the

removal of image distortions, and the improvement in overall sensitivity by improving the collections optics and adding a microchannel plate image intensifier to the CCD detector, and are discussed in the following chapters.

CHAPTER 5
RESONANCE RADIATION DIFFUSION IN ATOMIC VAPOR IMAGING

Introduction

Atomic line filters have been used in spectroscopic applications as devices that offer high spectral resolution and excellent background rejection. An atomic line filter, operating in either absorption or fluorescence modes, detects photons that lie within the spectral bandpass of an atomic line, which can be on the order of 1 GHz. The fluorescence line filter can be used as either a resonance fluorescence monochromator or a two-dimensional resonance fluorescence imaging monochromator (RFIM) capable of high-fidelity images with high spectral resolution. The spatial resolution of the RFIM is limited in theory only by the imaging system used to obtain the fluorescence image; for example, a charge-coupled device (CCD) camera pixel (approximately 10 μm x 10 μm). In practice, however, the best spatial resolution achieved is on the order of 300-500 μm. The reduced spatial resolution observed in atomic imaging filters results from several spectroscopic and geometric factors which are discussed below.

Palermo and Crouch [47] gave a mathematical treatment and experimental validation of resonance monochromators as detectors in atomic absorption spectrometry. Resonance fluorescence filters have also been used extensively as photon detectors in laser Doppler velocimetry [48,49]. Several atomic line filters have been developed based on elements that can be vaporized easily, such as potassium, calcium, sodium, mercury,

magnesium, rubidium, and cesium (see, for example [50-53]). One common trait shared by all these resonance filters is that they all involve an isolated atomic transition. In other words, a single transition excites the atom, and the atom then radiates *via* a resonance or step-wise transition. In most cases, the resonance line is also emitted, and the background rejection is degraded. Gelbwachs [54] has described a method of active-wavelength shifting in order to further excite the atoms in the atomic line filter, causing them to radiate from a different energy level. The increased selectivity gained by wavelength conversion gives the detector greater background rejection. The use of active wavelength shifting has been demonstrated in magnesium vapor [55,56].

The previous resonance fluorescence detectors all functioned as single-point measurement devices incapable of obtaining spatial information. Any atomic filter can, in principle, be used as a two-dimensional imaging device. A mercury resonance fluorescence imaging monochromator based on active-wavelength shifting was demonstrated [41] using a two-step excitation scheme. Two-step cesium resonance fluorescence monochromators have also been reported by Korevaar *et al.* [46] and Pappas *et al.* [57].

The spatial resolution reported by Matveev *et al.* [41], Hamadani *et al.* [46], and Pappas *et al.* [57] did not approach the theoretical limit for several reasons. Collisions with buffer gases, wall collisions, and thermal diffusion of excited atoms in the excitation/imaging region all contribute to losses in image fidelity. One source of broadening which has not been discussed in previous studies is the diffusion of resonance radiation. This distortion, caused by the resonance fluorescence from the excitation steps and radiation trapping in the pumping scheme, can severely limit the spatial resolution

obtained in an imaging filter. The RFIM described in chapter 4 [57] is used in this chapter to study the resonance radiation diffusion (RRD) effect. The RFIM described in that study had a minimum detectable number of photons of 10^{11} photons/cm^2, a linear dynamic range of 5 decades, and a quantum efficiency of 1%. The response time of the detector, which in the cw-excitation case was limited by the smallest spontaneous emission rate–the $6^2D_{5/2} \rightarrow 6^2P^o_{3/2}$ transition–was approximately 16 μs. The spectral resolution of the detector, limited by the Doppler linewidth of one hyperfine component of the 852.12 nm transition, was 400 MHz, and the spatial resolution obtained with the Cs RFIM in [57] was 200 μm at the optimum conditions.

The resonance radiation diffusion effect played a role in both resonance fluorescence imaging and resonance ionization imaging. Optimization of number density and laser irradiances (both signal and pump laser) minimized the RRD effect, providing the best spatial resolution of approximately 150 μm or less.

At higher Cs number densities, it is expected that radiation diffusion will have a large effect; in addition, the irradiance of both signal and pump lasers will also affect the overall spatial distortion. A compromise must be reached between the highest possible number density (in order to ensure complete absorption of the incoming photons), optimum laser irradiances, and the best spatial resolution. This is especially important in imaging filters with high atomic number densities, such as those based on alkali metals or other high vapor-pressure elements

Experimental Setup

The Cs RFIM used in this work has been described previously [57]; however, for the sake of completeness pertinent information will be restated and changes to the system

will be mentioned (Figure 5-1). Two cw diode lasers in Littman-Metcalf external cavities were used for the two-step excitation scheme (Figure 5-2). The first diode laser supplied light for the signal transition (at 852.12 nm ($6^2S_{1/2} \rightarrow 6^2P^o_{3/2}$), and had an output of 16

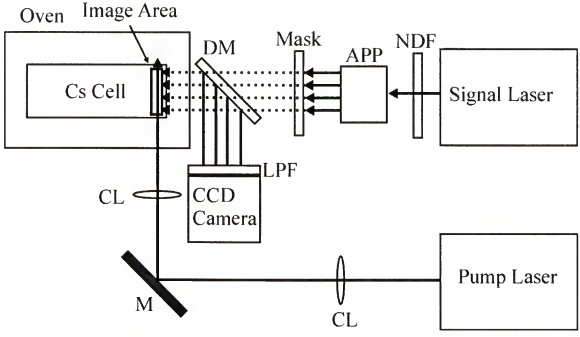

Figure 5-1. Experimental Setup of the RFIM, showing the imaging area in the cell. M = Mirror, DM = Dielectric Mirror, APP = Amorphic Prism Pair, NDF = Neutral Density Filter, LPF = Low Pass Filter, CL = Cylindrical Lens. Solid lines reflected from dichroic mirror indicate 455.53 nm fluorescence. CCD camera contains imaging lenses.

mW with a linewidth of approximately 5 MHz. The output of the laser passed through an amorphic prism pair to shape and slightly expand the beam (4 mm x 10 mm), which then passed through a stainless-steel mesh that served as the image source. The mesh transmission mask had bars of 270 μm width with a period of 420 μm. The image of the mesh was then passed through a dielectric mirror that transmitted near-infrared light and reflected visible.

The second laser was used as the pump (λ_2) laser at 917.23 nm ($6^2P^o_{3/2} \rightarrow 6^2D_{5/2}$). The λ_2 laser had an output power of 33 mW and a 5 MHz linewidth. This beam was

transformed into a sheet of light 12 mm long and 0.5 mm wide using a pair of cylindrical lenses. At the operating irradiances, the λ_2 laser output was sufficient to achieve saturation of the second step. This sheet of light entered the cell from the side, forming

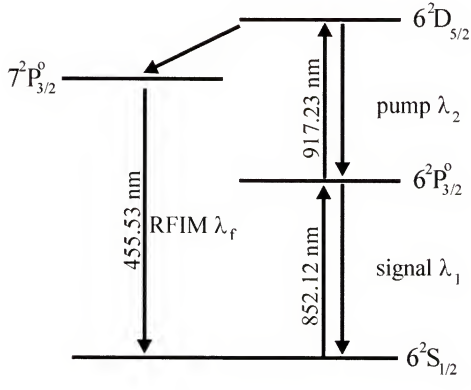

Figure 5-2. Partial energy level diagram of Cs showing the signal, pump, and fluorescence wavelengths.

the imaging plane parallel and close to the input window. Atoms pumped by the λ_2 laser to the $6^2D_{5/2}$ state decay to the $7^2P^o_{3/2}$ state *via* a radiative transition (14.35 μm, $6^2D_{5/2} \rightarrow 7^2P^o_{3/2}$) where they spontaneously returned to the ground state, emitting photons at 455.53 nm. The depth of the image formed in the RFIM was approximately the width of the λ_2 sheet of light.

A cylindrical pyrex RFIM cell (Opthos Instruments, Rockville, MD, USA) 75 mm in length with 25 mm diameter windows was used. The cell contained Cs metal under a vacuum. It was placed in a plexiglass box with a temperature—controlled nitrogen purge. The cell temperature was measured with a thermocouple placed near the cell.

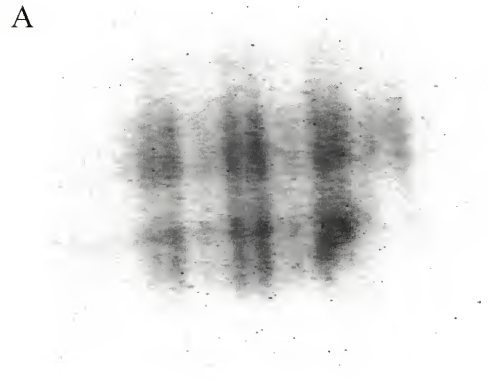

Figure 5-3. Images of the transmission mask at low Cs number density (10^{10} cm^{-3}). Darker color represents higher fluorescence intensity.

The dielectric mirror used to pass the image photons also collected the blue fluorescence from just behind the input window. The imaging plane was less than 0.5 mm from the input window, and the absorption coefficients for λ_1 and λ_f fluorescence were 1.92 cm^{-1} and 0.014 cm^{-1}, respectively. This ensured that the majority of the λ_1 image photons were absorbed in the imaging area but the blue 455.53 nm fluorescence passed out of the

cell without much attenuation. The blue fluorescence was collected through a 650 nm low-pass filter (80% transmission at 455.53 nm) into a digital CCD camera (Model Cybershot DSC-S70, Sony, Japan) with an 8 s integration time. This camera was interfaced to a computer. Images were processed using SigmaScan software (SPSS, Chicago, IL, USA).

B

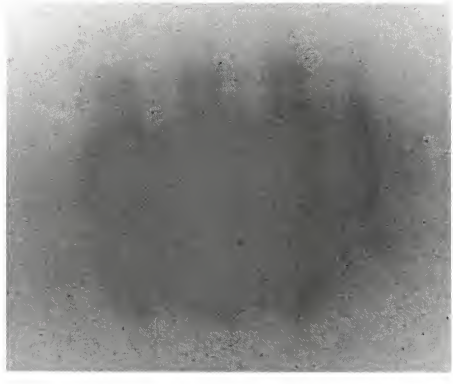

Figure 5-3 Continued. Image of the transmission mask at high Cs number density (3×10^{11} cm^{-3}).

Results

Number density effects. The temperature of the plexiglass oven was varied in order to study the RRD effect as a function of the number density of ground-state cesium atoms. The temperature was varied from 20.3–45.0 °C, which corresponded to a number density range of 3×10^{10} cm^{-3}–3×10^{11} cm^{-3}. Images were acquired after the cell was

allowed to equilibrate. Figure 5-3 shows two images taken at a number density of 6 x 10^{10} cm^{-3} (Figure 3a) and 2 x 10^{11} cm^{-3} (Figure 3b). In Figure 5-3a, the bright sections of the image are resolved; however, in Figure 5-3b the spatial distortion due to radiation trapping is clearly observed. In order to quantify the degree of distortion, the ratio of the signal (taken as the center of the dark areas of the image) to the background (taken as the center of the bright areas of the image corresponding to a bar on the mesh) was

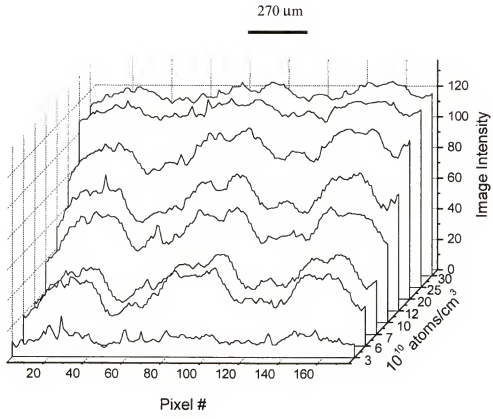

Figure 5-4. Point spread functions of the mesh images as a function of Cs number density.

calculated. Signal and background measurements were obtained from point spread functions acquired along a section of the images. Point spread functions of the images, acquired using the SigmaScan Pro software package, are shown in Figure 5-4.

Figure 5-4 shows that the overall fluorescence intensity increases; however, the degree of radiation diffusion also increases.

The signal-to-background ratio, S/B, which was measured for each point spread function, is shown in Figure 5-5. It can be seen that as the number density is decreased, radiation diffusion also decreased and the signal-to-background increased. There is a practical limit, however, where the number density is too small to produce a detectable

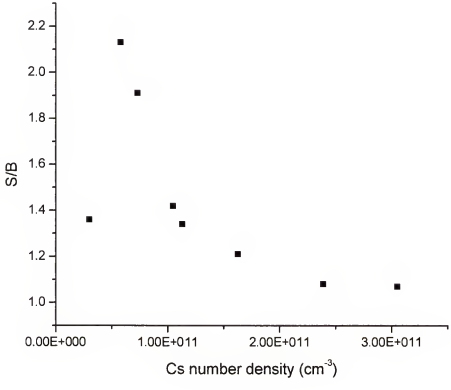

Figure 5-5. Signal-to-background ratios of the point spread functions shown in Figure 5-4.

image with the current CCD camera system. It is anticipated that once the cell is cooled below room temperature and is no longer an optically thick medium, decreasing the number density further will not improve the spatial resolution. At the optimum S/B ratio

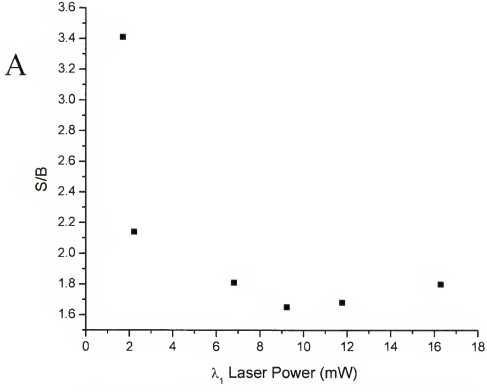

Figure 5-6. Signal-to-background ratio as a function of the signal laser power.

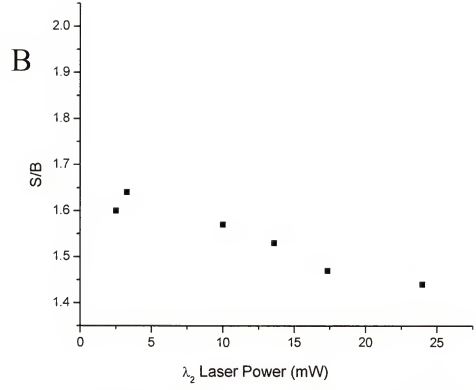

Figure 5-6 Continued. Signal-to-background ratio as a function of the pump laser power.

at 6 x 10^{10} cm^{-3}, the optical density of the RFIM for λ_1 photons was sufficient to acquire images with high sensitivity.

Signal (λ_1) and pump (λ_2) laser effects. The irradiances of both the signal and pump lasers also contributed to the overall spatial distortion. The RFIM cell was set at the optimum number density obtained from the previous measurements, approximately 6 x 10^{10} cm^{-3}, and laser output for each laser was separately attenuated using a set of neutral density filters. The same point spread function and S/B measurements were made for each image. The dependence of S/B on the signal (λ_1) laser output power is shown in Figure 5-6a, and the plot of S/B as a function of pump (λ_2) output is shown in Figure 5-6b. It is clear that the signal output power contributes to the spatial distortions observed in the images. The pump laser power, however, did not cause a large change in the S/B, possibly because the RFIM signal decreased before any increase in S/B is observed. In routine practice, such as in the measurement of faint sources, the pump laser has enough power to saturate the $6^2P^o_{3/2} \rightarrow 6^2D_{5/2}$ transition, but the signal photons will originate from a sufficiently weak source so the RRD effect from the lasers will be minimal. Therefore, optimization of the RFIM with respect to spatial resolution will be a compromise between a high number density and a high signal-to-background ratio. At the optimum parameters used in this study, the best spatial resolution obtained was less than 150 μm.

Conclusion

The observation and quantification of resonance radiation diffusion are reported. The RRD effect, which is responsible for the degradation of image fidelity and spatial resolution, is found to cause the greatest distortion at high number densities and signal

laser power. The RRD effect will degrade images in any type of atomic fluorescence or ionization filter, and care must be taken to ensure that the operating parameters are chosen to maximize the spatial resolution. The effect of resonance radiation diffusion was demonstrated in a Cs RFIM in order to measure the loss of spatial resolution in the imaging detector. While other effects cause spatial distortion, such as collisions with foreign gases and cell walls, the thickness of the imaging region (defined by the thickness of the λ_2 sheet of light, and isotropic emission from the imaging region, the RRD effect is one that can be readily minimized with careful optimization of operating parameters.

CHAPTER 6
DETECTION OF SINGLE PHOTOELECTRONS IN A RESONANCE FLUORESCENCE IMAGING MONOCHROMATOR.

Introduction

There has been recent interest in spectroscopic applications for high-fidelity image acquisition to increase the information content in a measurement. In applications requiring high spectral resolution (less than 0.01 nm), there are few devices that can be used for spectroscopic imaging. Examples include scanning heterodyne detectors [58], scanning line imaging monochromators based on diffraction gratings [6], Fabry-Perot type imaging filters [4], and atomic imaging filters [54,56,45]. While many of these filters achieve high spectral resolution, it is difficult to acquire an image without the use of scanning, which increases the measurement time. The atomic imaging filter, however, can be used to acquire macroscopic and microscopic images with high fidelity using global illumination. In addition to the capability of true image acquisition, the atomic imaging filter, such as a resonance fluorescence imaging monochromator (RFIM), has a spectral resolution limited by the Doppler-broadened or natural-broadened (in Doppler-free conditions) linewidth of the atomic vapor used, which can be much narrower than grating monochromators or Fabry-Perot filters. In many spectroscopic devices, such as heterodyne detectors, the resolution can be very high, but the throughput of the system can degrade the sensitivity of the detector.

One method for comparing spectral imaging devices is the luminosity-resolving power product, LR. It has been shown [59-60] that the LR product is a universal method for comparing imaging filters in order to assess the resolving power and overall throughput of the detector. The LR product is also shown to be proportional to the square of the signal-to-noise ratio $(S/N)^2$ of an imaging system. The LR product, therefore, can indicate the overall sensitivity of the imaging device as well. The LR product of the RFIM (approximately 10^7 cm^2/sr) is several orders of magnitude larger than a Fabry-Perot filter (10^3 cm^2/sr), grating imaging monochromator (1 cm^2/sr), or heterodyne detector (10^{-8} cm^2/sr) [60]. It is evident that the RFIM has a LR product that is 4 orders of magnitude large than many other techniques used for high resolution imaging.

A Cs-based RFIM [57] has been demonstrated as a spectrally-selective imaging detector with a spectral resolution of 400 MHz (0.97 pm at 852.12 nm) and a spatial resolution less than 150 nm [61]. The sensitivity of this detector, however, has not been demonstrated. In this chapter, the detection of a single RFIM fluorescence photon, corresponding to an input signal of 10^4 photons within the bandpass of the detector, is reported.

Experimental Setup

The experimental setup has been described in chapter 5 and elsewhere [57]. The beam from a continuous wave (cw) external cavity diode laser was attenuated using neutral density filters so that the output power was sufficiently low to ensure that a random distribution of photons was achieved. The laser beam was tuned to the signal frequency of the RFIM corresponding to the $6^2S_{1/2} \rightarrow 6^2P^o_{3/2}$ transition of cesium (852.12 nm). This beam was collimated and expanded using an amorphic prism pair, and then

passed through a USAF 1951 resolution target mask. The image from this mask was collected with an F/4.3 lens and focused onto the image plane of the RFIM, which was formed by a planar sheet of laser light from the cw external cavity pump laser. The pump laser transition corresponded to the $6^2P^o_{3/2} \rightarrow 6^2D_{5/2}$ transition of cesium (917.23 nm), and the output power of the laser was sufficient to saturate the transition. Atoms pumped to this state then radiatively relaxed to the $7^2P^o_{3/2}$ state and then fluoresced to the ground state via the 455.53 nm transition line. The 917.23 nm laser beam was transformed into a sheet of light, which entered the cell parallel to and just behind the input window of the cell. The fluorescence from the cell was imaged with an F/1.4 lens onto the photocathode of an image intensifier tube (Hammamatsu, Japan) using a dichroic mirror on the front surface (see Figure 6-1). The amplified image was then acquired using a cooled CCD camera (Model Penguin 150CL, Pixera Corp. Los Gatos, CA). Images were acquired using the camera software and analyzed using SigmaScan Pro software. A cylindrical pyrex cell containing cesium was used and operated at 20.3 ^oC, which corresponded to a Cs atom number density of 3 x 10^{10} cm^{-3}. The entire system was encased in a black plexiglass enclosure that served to eliminate ambient light. Both the incoming signal radiation (at or near 852.12 nm) and the pump laser sheet passed through 750 nm longpass filters to enter the enclosure.

Results

Spatial Distribution of Single Photoelectrons. An area of the image of the USAF mask that corresponded to transmitted 852.12 nm light was taken as the measurement area, which corresponded to 90 x 84 pixels. The signal due to single photoelectrons was

readily distinguished from the background signal due to stray light. In order to determine whether to photoelectrons were randomly oriented in space, 6 successive images were obtained. Each image had a grid consisting of 20 sections overlaid on the image, and the

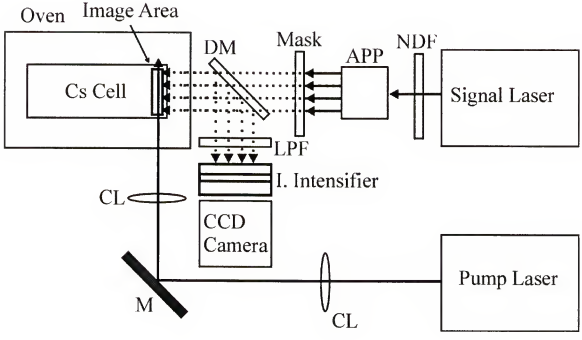

Figure 6-1. Experimental Setup of the RFIM. NDF = Neutral density filter, APP = amorphic prism pair, Mask = USAF bar target, DM = dichroic mirror, LPF = long pass filter, CL = cylindrical lens used to form sheet of light. Lens in front of image intensifier is not shown.

number of photoelectrons per grid were counted. The signal from a single photoelectron was 4 times larger from surrounding, background pixels. The number of photoelectrons per grid area appear in Figure 6-2. It can be seen that the probability of detecting more than one photoelectron in a grid area decreases rapidly.

In order to determine whether the photoelectron events indeed occur randomly, the data set was subjected to a chi-squared (χ^2) test in order to determine if the system is

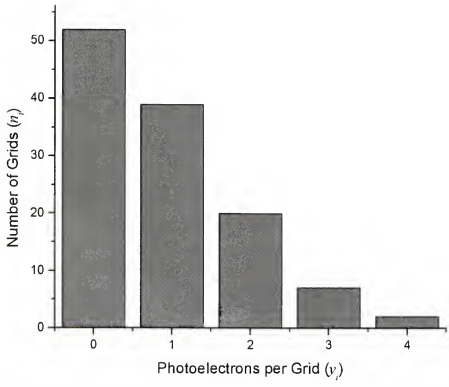

Figure 6-2. Plot of the number of photoelectrons found in the measurement grids of an image, and the number of grids that contain y_i photoelectrons.

truly Poissonian [62]. The null hypothesis, H_0, states that observed photoelectrons all come from a common Poissonian distribution with unspecified μ. The assumptions in this calculation are as follows:

1. Photoelectron events do not occur at the same point in space.
2. The photoelectron events are independent of each other.
3. The number of photoelectron events that occur in a specific time interval, Δt, is the same for all other intervals of Δt.

The image intensity was sufficiently low to ensure that the photoelectrons were not detected at the same point in space, and measurement of the individual photoelectron

intensity indicates that all of the photoelectrons are of the same intensity. Since the photons emitted at the blue (455.53 nm) wavelength are from different Cs atoms, the emission events are independent of each other. Third, the number of photoelectrons measured in all of the images was approximately the same, indicating that in the exposure time of the camera, the same number of photoelectrons were detected.

The chi-squared (χ^2) value that determines if the null hypothesis can be rejected can be calculated from the following formula [62]:

$$\chi^2 = \sum_i \left[\frac{(n_i - E_i)^2}{E_i} \right], \tag{6-1}$$

where n_i is the number of grids in the image containing y_i photoelectrons (in this case, y_i = 0, 1, 2, 3, 4), E_i is the expected number of photoelectrons in grid i (defined below). E_i is valid for a given confidence interval, α, and a given number of degrees of freedom, d.f. (where d.f. = k-2, and k is the number of E_i's). The values of n_i and y_i are given in table 6-1. In order to calculate the values of E_i for each grid i, the Poisson parameter, μ, must be calculated (here μ is equivalent to the mean number of photoelectrons, $\bar{y}$). The parameter $\bar{y}$ can be defined as follows:

$$\bar{y} = \mu = \frac{\sum_i (n_i y_i)}{n}, \tag{6-2}$$

where n is the number of grids (n = 120 in this case). $P(y_i)$ values are tabulated for a given Poisson probability (see Table 6-1 for the $P(y_i)$ values used). The Poisson probability is used to calculate the E_i value, as $E_i = n\,P(y_i)$. For this method to be valid E_i >1 and not more than 20% of the E_i values should be less than 5. Using the compiled values for n_i and E_i, the χ^2 value is 1.6. For a confidence interval of 95% (1-α), and 3

degrees of freedom (since there are 5 values of E_i), the tabulated χ^2 value is 7.8. Since the calculated χ^2 value is less than the tabulated value, there is insufficient evidence to reject the null hypothesis. The distribution of the photoelectrons in this case is Poissonian, and are due to random, single photoelectron events.

Table 6-1. Experimental and calculated parameters used to determine the χ^2 value.

y_i	0	1	2	3	4
n_i	52	39	20	7	2
$P(y_i)$	48.0	44	19.2	6.0	1.2

Amplification effects on single photoelectron detection. In order to determine whether single photoelectrons were truly being detected, the gain on the image intensifier was varied while observing the intensity of the image. Figure 6-3a shows the signal from a more intense signal where multiple photoelectrons were measured at each pixel. The image intensity increases linearly with the gain voltage of the image intensifier, which is to be expected for a relatively bright image. When the image intensity is so low that the photoelectron signal is random, the image intensity dependence on gain should be different. The number of photoelectrons observed in the 90 x 84 pixel volume as a function of gain voltage is shown in Figure 6-3b. At lower gain voltages, the image is dark and no photoelectrons are detected. As the gain is increased, the image remains dark until a threshold voltage is reached. At that point increasing the amplification does not increase the number of photoelectrons amplified image intensifier. This result

indicates that the intensifier does not detect more photons, and that the photoelectrons imaged by the CCD are due to single, random photon events.

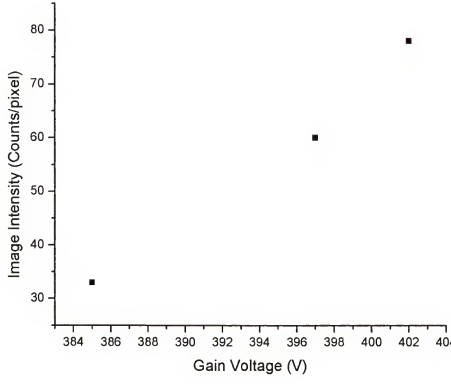

Figure 6-3. The image intensity of a relatively bright image as a function of the gain voltage of the image intensifier.

Conclusion

The measurement of single fluorescence photons from the output of a resonance fluorescence imaging monochromator has been demonstrated. The random appearance of photons during the CCD exposure time was demonstrated by fitting the results to a Poissonian distribution, as well as studying the amplification effects on the photoelectron

signal. The detection of a single photoelectron, however, does not indicate that only one photon was absorbed by the atomic vapor. One must consider the total collection efficiency of the RFIM to estimate the total number of photons required to generate a single photoelectron. This estimate gives the ultimate limit of detection of the RFIM.

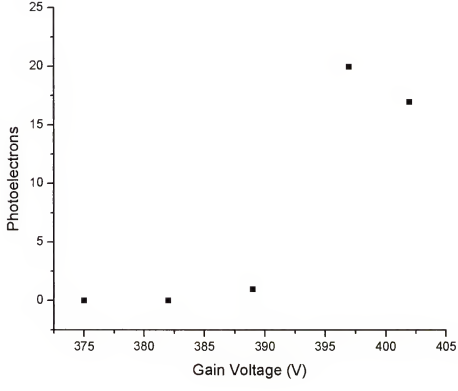

Figure 6-3 (cont). The number of photoelectrons from a faint image as a function of the gain voltage of the image intensifier.

Photons that enter the enclosure through the longpass filter (0.8 transmission) are further attenuated by the dichroic mirror (T = 0.90). The photons that enter the cell are absorbed by the cesium vapor, and the excited-state atoms in the pumping volume (10%) are then excited to the $6^2D_{5/2}$ state and fluoresce via the 455.53 nm transition with 1%

conversion efficiency. The F/1.4 lens collects approximately 2.7% (accounting for the reflectance of the dichroic mirror) of the isotropically emitted light and forms an image on the image intensifier photocathode (having a 40% quantum efficiency). Using these values, we can estimate that for every 10^4 photons that enter the RFIM 1 photoelectron is detected by the CCD camera. The total detection efficiency, therefore, is 0.01%, which is orders of magnitude larger than other imaging detectors such as grating monochromators and heterodyne imaging systems. Improving the conversion efficiency of the RFIM, and using lower F-number collection optics could lower the LOD of the detector.

While the limit of detection for a single point in space is 10^4 photons (2 fW at 852.12 nm), the limit of detection for an image is higher. It is difficult to place an exact value on the minimum number of photons required to generate an image, because the number of pixels required to generate an image that is distinguishable from the noise is not defined. In the case where only 100 pixels are needed to distinguish the features of an image, a limit of detection of 200 fW of 852.12 nm light can be estimated. With higher resolution imaging, the limit of detection increases with the number of pixels. The threshold of image pattern perception and recognition is, therefore, impossible to assign, and the limit of image detection will be difficult to assess. The limit of detection of a single pixel, however, is a valid figure of merit describing the capabilities and limits of an imaging system.

CHAPTER 7
DETECTION OF MIE SCATTER USING A RESONANCE FLUORESCENCE DETECTOR

Introduction

The use of an atomic vapor filter as a narrowband source for high resolution spectral imaging has proven to be an efficient method of photon detection [57, 40]. One of the proposed applications of atomic vapor filters is Rayleigh and Mie scattering spectroscopy. Rayleigh and Mie scattering spectra yield a great deal of information on the physical state of many environmental, industrial, and biological samples (e.g. temperature, particle density). There are many different methods of acquiring scattering spectra from particles and fluids, all requiring high quantum efficiency and spectral resolving power. Atomic resonance filters have been used in previous studies to discriminate between Mie and Rayleigh spectra [63-64], or to resolve both Rayleigh and Mie spectra *via* deconvolution methods [65]. These studies used an atomic vapor filter as a rejection filter. In other words, the cell was used in the absorption mode, providing little spectral selectivity in comparison with a two-step excitation/fluorescence scheme.

Using a two-step fluorescence scheme offers several advantages in the detection of scattered light. Resonance radiation that is scattered from interfaces such as lenses and cell walls is not be detected by the CCD or photomultiplier tube that detects the RFIM output. Surface scatter and other stray light are effectively rejected in this method. Another advantage of using a two-step scheme is that the spectral response can be limited

to one hyperfine line of the Cs ground state, thereby improving the spectral resolution to approximately 400 MHz or less. A third advantage is that fluorescence experiments are inherently more sensitive than absorption experiments.

Experimental Setup

In this chapter, the Mie scattering spectrum of silica particles suspended in solution was detected using a deconvolution method. The resonance fluorescence imaging monochromator was operated in nonimaging mode; the entire fluorescence signal was collected without regard to the spatial information obtained from the RFIM. The experimental setup was identical to that described in Chapter 6 of this work, however, a photomultiplier tube (R928, Hammamatsu, Japan) was used instead of the image intensifier/CCD camera to detect the 455.53 nm fluorescence. The PMT current was amplified using a transimpedance amplifier, and the voltage output was displayed and stored on a digital storage oscilloscope (TDS 3012, Tektronix, Inc. Wilsonville, OR). Figure 7-1 shows the experimental setup for the scattering experiments.

The signal laser passed through a glass cuvette containing the scattering sample. The sample was a suspension of silica particles (Bangs Laboratories, Fishers, IN) with a concentration of 3.54 $x10^9$ particles/cm^3 and a 400 nm particle diameter. The stock solution was kept refrigerated to suppress bacterial growth, which could affect the particle diameter and Mie scattering cross section. The pump laser entered the cell orthogonally to illuminate the entire 1:1 image of the scatter formed in the Cs cell with 917.23 nm light. This beam geometry corrected for any errors in beam overlap and provided the maximum laser interaction area with a high irradiance (0.5

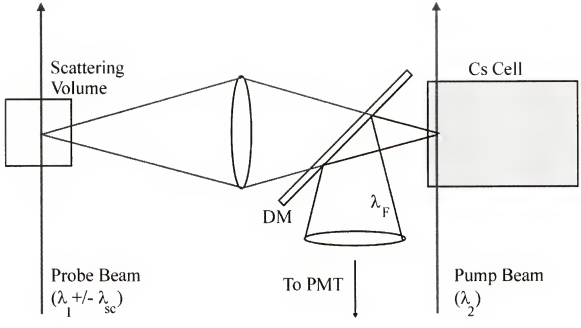

Figure 7-1. Experimental Setup of the Mie scattering experiment. DM = Dichroic Mirror.

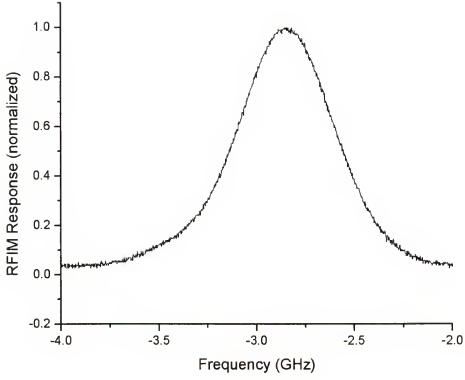

Figure 7-2. Frequency Response of the RFIM.

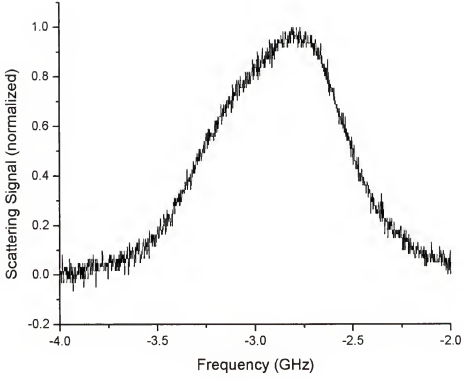

Figure 7-3. The convoluted Mie scatter signal.

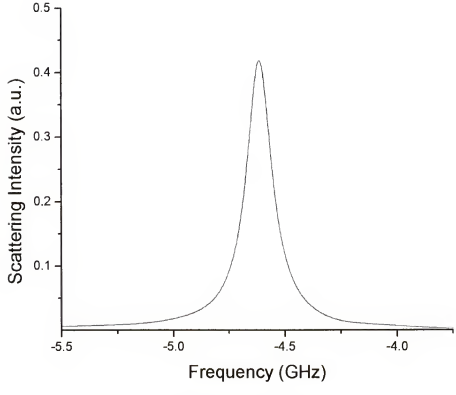

Figure 7-4. The deconvoluted Mie spectrum. The full-width at half maximum is 150 MHz.

W/cm^2). The resulting 455.53 nm fluorescence was then collected into the PMT. The signal laser was scanned over a 10 GHz range using a function generator that also triggered the oscilloscope. Digitized waveforms were processed and deconvoluted using Origin software (Origin 5.0, OriginLab Corp., Northhampton, MA).

Results

The spectral response of the RFIM is shown in Figure 7-2. The linewidth of the fluorescence is approximately 500 MHz, which is the Doppler-broadened linewidth of the $6^2S_{1/2} \rightarrow 6^2P^o_{3/2}$ hyperfine lines pumped by the λ_2 laser. Comparing Figure 7-2 with the measured Mie spectrum (Figure 7-3), only a slight difference (200 MHz) in the linewidth is observed. Using deconvolution software, the Mie spectrum was obtained (see Figure 7-4).

Because the RFIM response is broader than the Mie scattering linewidth, there is the possibility that the Mie spectrum will be distorted, and that much of the spectral information will be lost. This occurs primarily when the noise level in the measured signal is very high. Mie scatter spectra have a line shape that approximates a Gaussian function, and fitting the deconvoluted Mie spectrum to a Gaussian function can reconstruct any lost information [65]. In our case, the noise level is sufficiently low and the Mie scatter is resolved.

It is important to note that there is not an observable signal from the Rayleigh scatter. At the high concentration of particles used in this study, the Mie scatter signal was several orders of magnitude larger than the Rayleigh signal. In order to observe Rayleigh scattering signals, the gain of the system must be increased beyond the saturation limit of the detector for the Mie scatter, and will cause distortions in the

obtained spectrum. Rayleigh spectra can be detected using a RFIM, however, and simultaneous Rayleigh and Mie spectra can be measured when the signals differ by only a few orders of magnitude.

Conclusion

The RFIM has been demonstrated as a device for detecting narrowband signals from a scattering source. While the FWHM of the Mie scatter is narrower than the RFIM spectral response, the difference in the RFIM and Mie linewidths is small enough to allow deconvolution methods to extract the desired data. The linewidth of the Rayleigh spectrum is 140 MHz, and agrees well with theoretical values (100 MHz for particles in air) [65]. The detection of Mie scattering using the RFIM is a preliminary experiment to demonstrate the ability to detect narrowband signals with the RFIM.

CHAPTER 8
FINAL COMMENTS

Conclusions

The design evaluation, and implementation of a cesium-based resonance fluorescence imaging monochromator has been described. The physical environment of the atomic vapor filter was studied in an effort to understand the mechanisms of loss in an resonance fluorescence detector. The collisional excitation and ionization of Cs atoms by Ar buffer gas was found to depopulate the $6^2P^o_{3/2}$ state, creating a large loss of signal in the atomic vapor.

A key disadvantage of this loss mechanism is that the atoms that could be pumped by the 917.23 nm laser to cause a fluorescence signal at 455.53 nm are instead distributed over a large range of atomic energy levels. The radiated light occurs over a large spectral window, making it difficult to filter the desired light from interferences such as room light. In addition, the ionization is due to a one-step excitation, which is not as selective as a multi-step excitation. For example, resonance light at the 894.35 nm transition (see Figure 2-4) can also create a plasma under the same conditions, while these same photons will not generate a signal in a RFD lacking a buffer gas. By reducing the buffer gas pressure or removing the gas altogether, the plasma mechanism can be suppressed. In addition, Cs atoms are known to cause associative ionization at high number densities, and this is evident in the nonlinear dependence on the Cs atom concentration on plasma

formation. Keeping the cell operating temperature sufficiently low can remove these negative effects as well.

While collisional ionization had been reduced by lowering the Cs number density, the collisional mixing of 6^2P_J and 6^2D_J levels also provided loss mechanisms in the Cs RFD. Collisional mixing was present regardless of Ar buffer gas concentration, although the pressure of the buffer gas did affect the degree of mixing. The effect of collisional mixing of the Cs fine structure levels was modeled using the density matrix formalism. The collisional mixing rates of the atomic vapor cell used were obtained by comparing simulation results to experimentally observed fluorescence intensities, and the mixing behavior of the system was predicted. By removing the buffer gas from the cell, collisional mixing was no longer present. Using a cell containing Cs under a vacuum at temperatures below those required for plasma formation ensured that the majority of nonradiative losses (ionization, mixing, collisional excitation) were removed.

In a cell containing only cesium, however, there are enough collisions between ground state Cs atoms to ensure that optical pumping, in which one of the hyperfine levels of the ground state is depleted, does not occur. This is due to the relatively large number density in comparison to magneto-optical traps that are conventionally used to observe optical pumping. The depletion of the ground state due to optical pumping would reduce the efficiency of the RFIM by several orders of magnitude. Using the evacuated Cs cell, a resonance fluorescence imaging monochromator was developed. The RFIM benefited from the improved efficiency gained by reducing the loss mechanisms in the cell, and demonstrated both the spectral selectivity and spatial resolution of the detector. The RFIM was able to obtain two-dimensional images with a

spatial resolution of approximately 200 μm. The response of the detector was found to be linear as long as the signal laser was kept below the saturation irradiance of the atomic vapor. The spectral response of the cell was limited by the Doppler-broadened linewidth of a single hyperfine component of the $6^2S_{1/2} \rightarrow 6^2P^o_{3/2}$ transition (400 MHz). The attenuation factor for out-of-band radiation was high (>99% at $\Delta\nu_1$ = 1GHz), and is limited primarily by noise in the CCD camera. The quantum efficiency was calculated to be approximately 1%, with a total collection efficiency of 0.05%, which is on the order of the efficiency obtained with typical broadband imaging systems. The spectral resolution was orders of magnitude higher than that obtained with conventional imaging and photon detecting devices.

The spatial resolution of the RFIM was limited by several factors, primarily the diffusion of resonance radiation. Radiation diffusion was observed as the cell was heated from room temperature to the normal operating temperature of 40 ^oC. The spectral resolution worsened as the temperature–and Cs number density–as increased. The signal to background ratio of images was seen to decrease as radiation diffusion blurred the fluorescence signal over the image area. Optimal conditions were found with room temperature cells, because the radiation trapping was minimized but there were still enough Cs atoms in the cell to absorb essentially all of the incoming signal photons. The signal and pump lasers were also found to affect the degree of radiation trapping, but their effects are minimal under normal operating conditions.

The sensitivity of the RFIM was also demonstrated by detecting single photoelectrons from the image intensifier used for image signal amplification. These single photoelectrons were found to occur randomly, and corresponded to low light levels

impinging on the RFIM input. For a single photoelectron, the theoretical limit of detection was 10^4 photons of 852.12 nm light per pixel of the imaging detector.

In order to demonstrate the spectral resolution of the RFIM, Mie scattering was detected from a scattering medium. The Mie signal, which is relatively narrow with respect to the frequency response of the detector, is extracted using deconvolution methods. The linewidth of the Mie scatter agrees well with the theoretical value. The RFIM can be used to detect a variety of narrowband signals, and the application to Mie scattering was a preliminary step to demonstrate the effective resolution of the detector.

Future work

While the spatial resolution, spectral resolution, and quantum efficiency have been studied in detail, further improvements and applications must be made to the detector. One of the key improvements that could be made to the RFIM is to decrease the absorption linewidth of the atomic vapor and achieve sub-Doppler-broadened line profiles. By reducing the absorption linewidth, and at the same time the spectral resolution of the detector, applications such as Doppler velocimetry of slower-moving objects are possible. It should be noted that the reduction in spectral line profile is not necessary for all applications, and the spectral resolution must be chosen to suit the application. The reduction of Doppler-broadened linewidths could be achieved using the well-established technique of single-step saturation spectroscopy; however, this is not practical in the case of an atomic vapor detector, as the saturating beam used to generate the sub-Doppler signals will generate large resonance fluorescence signals, which could obscure any signal photons at 852.12 nm.

There are two other methods that can be used to reduce the effective spectral resolution of the imaging detector. The first method is relatively simple and can be used without additional equipment. In the current experimental setup (see chapters 6-7), the sheet of light from the pump (λ_2) laser excites the atoms in an orthogonal direction with respect to the incoming signal (λ_1) photons. The spectral linewidth of the RFIM is limited by the total linewidth of the Doppler-broadened hyperfine absorption line (in this case, atoms in the F = 4 hyperfine level of the ground state which are then pumped to the F = 3,4,5 hyperfine levels of the $6^2P^o_{3/2}$ state). If the pump beam is directed into the cell so that it either co-propagates or counter-propagates with the signal photons, then saturation effects can effectively reduce the Doppler linewidth. In the ideal situation, the RFIM resolution would be limited by either the natural linewidth of the 852.12 nm resonance transition (5.2 MHz) or the linewidth of the pump laser. In practice, however, the incoming signal photons will not be collimated in order to form an image, and the divergence of that signal beam will cause a broadening of about 150 MHz [66]. Placing the object to be detected far from the RFIM would ensure near-collimation of the image light, but the reduced solid angle of collection will decrease the sensitivity of the instrument. Work is now in progress to reduce the absorption linewidth using this method in both imaging [66] and nonimaging modes [67].

A more complicated method of linewidth reduction is the use of a prefilter that has a narrow linewidth, such as a Cs vapor cell under the conditions of electromagnetically-induced transparency (EIT) [68-72]. EIT occurs when a drive laser (λ_D) is used to induce a quantum interference between two states. If the signal beam shares a common level with the drive laser, then there will be a large reduction in the

absorption profile of the vapor. Several papers have been published on the EIT effect in cesium vapor [73-74]; however, the application of a cell under EIT conditions to atomic vapor filters has not been reported to this date.

Electromagnetically induced transparency can be used in an atomic vapor filter by placing an additional Cs cell in front of the RFIM cell. The first cell, which will undergo EIT, is the pre-filter cell. The pre-filter will, in the absence of the drive laser, have an absorption profile that is identical to the RFIM cell. If the drive laser is turned off, all of the photons that could be absorbed by the RFIM cell are instead absorbed by the pre-filter cell. By tuning the drive laser to resonance–in this case the drive laser will be tuned to the $6^2S_{1/2}$ (F=4) $\rightarrow$ $6^2P^o_{1/2}$ (F=3,4) transition of cesium at 894.35 nm–the transmission of the pre-filter cell will increase over a spectral interval that resembles the drive laser profile (5 MHz using an external cavity diode laser). The increase in transmission is large (up to 100%), creating an effective linewidth of the total RFIM system that can be on the order of the natural linewidth. Work has already begun to realize this proposed method of linewidth reduction.

The RFIM must also be improved from the preliminary system described in this work. The sensitivity of the instrument, which can be improved by either radiation trapping or heating the cell, must be optimized with respect to the spatial resolution, which will decrease as the Cs number density increases. The increase in sensitivity of the detector will enable the RFIM to detect lower light levels, and increase the applicability of atomic vapor filters to spectroscopic imaging.

REFERENCES

1. O.I. Matveev, B.W. Smith, J.D. Winefordner, *Appl. Optics*, **36**, 8833 (1997).

2. E.N. Lewis, P.J. Treado, I.W. Levin, *Appl. Spectrosc.*, **47**, 539 (1993).

3. H.R. Morris, C.C. Hoyt, P.J. Treado, *Appl. Spectrosc.*, **48**, 857 (1994).

4. K.A. Christensen, N.L. Bradley, M.D. Morris, R.V. Morrison, *Appl. Spectrosc.*, **49**, 1120 (1995).

5. D.M. Pallister, A. Govil, M.D. Morris, W.S. Colburn, *Appl. Spectrosc.*, **48**, 1015 (1994).

6. C.J. de Grauw, C. Otto, J. Greve, *Appl. Spectrosc.*, **51**, 1607 (1997).

7. J. Ma, D. Ben-Amotz, *Appl. Spectrosc.*, **51**, 1845 (1997).

8. G.J. Puppels, M. Ground, J. Greve, *Appl. Spectrosc.*, **47**, 1256 (1993).

9. M.A. Shannon, X.L. Mao, A. Fernandez, W.-T. Chan, R.E. Russo, *Anal. Chem.* **67**, 4522 (1995).

10. R.M. Measures, N. Drewell, P. Cardinal, *Appl. Optics*, **18**, 1824 (1979).

11. D.R. Lide (ed.), *CRC Handbook of Chemistry and Physics*, 75th edition, CRC Press, London (1995).

12. R. Gupta, W. Happer, J. Wagner, E. Wennmyr, *J. Chem. Phys.*, **68**, 799 (1978).

13. D.H. Sarkisyan, A.S. Sarkisyan, A.K. Yalanusyan, *Appl. Phys. B*, **66**, 241 (1998).

14. G.J. Havrilla, S.J. Weeks, J.C. Travis, *Anal. Chem.*, **54**, 2566 (1982).

15. C.Th.J. Aklkemade, Tj. Hollander, W. Snelleman, P.J.Th. Zeegers, *Metal Vapours in Flames*, Pergamon Press Ltd., New York (1982).

16. N. Omenetto, G.C. Turk, M. Rutledge, J.D. Winefordner, *Spectrochim. Acta Part B*, **42**, 807-817 (1987).

17. O. Axner, M. Norberg, H. Rubinsztein-Dunlop, *Spectrochim. Acta Part B*, **44**, 693 (1989).

18. N. Omenetto, RIS proceedings, Institute of Physics Conference Series, **128**, 151 (1992).

19. G.A. Petrucci, C.L. Stevenson, B.W. Smith, J.D. Winefordner, N. Omenetto, *Spectrochim. Acta Part B*, **46**, 975 (1991).

20. J.B. Simeonsson, K.C. Ng, J.D. Winefordner, *Spectrochim. Acta Part B*, **48**, 131 (1993).

21. T.Kakinuma, M. Fujii, M. Ito, *Chem. Phys. Lett.*, **140**, 427 (1987).

22. M. Fujii, T. Ebata, N. Mikami, M. Ito, *J. Phys. Chem.*, **88**, 4265 (1984).

23. Y. Anezaki, T. Ebata, N. Mikami, M. Ito, *Chem. Phys.*, **97**, 153 (1985).

24. N. Omenetto, M. Leong, C.L. Stevenson, J. Vera, B.W. Smith, J.D. Winefordner, *Spectrochim. Acta Part B*, **43**, 1093 (1988).

25. O. Marago, D. Ciampini, F. Fuso, E. Arimondo, C. Gabbanini, S. T. Manson, *Phys. Rev. A*, **57**, R4410 (1998).

26. H. Maeda, F. Ambe, *Phys. Rev. A*, **56**, 3719 (1997).

27. P. Ljungberg, "The Density Matrix Model for two-step LEI and LIF spectrometry," Internal Report (Chalmers University of Technology, Goteborg, Sweden, 1990).

28. J.B. Simeonsson, B.W. Smith, J.D. Winefordner, N. Omenetto, *Appl. Spectrosc.*, **45**, 521 (1991).

29. D. Boudreau, P. Ljengberg, O. Axner, *Spectrochim. Acta Part B*, **51**, 413 (1996).

30. E. Voigtman,, *Spectrochim. Acta Part B*, **48**, 625 (1993).

31. I. Hirano, *Opt. Comm.*, **57**, 331 (1986).

32. A. Sasso, W. Demtroder, T. Colbert, C. Wang, E. Ehrlacher, J. Huennekens, *Phys. Rev. A*, **45**, 1670 (1992).

33. A.A. Radzig, B.A. Smirnov, *Reference Data on Atoms, Molecules, and Ions*, Springer-Verlag, New York (1985).

34. O.I. Matveev, *J. Appl. Spectrosc. (USSR)*, **46**, 217 (1987).

35. R.J. Krupa, G.L. Long, J.D. Winefordner, *Spectrochim. Acta Part B*, **40**, 1485 (1985).

36. T. Okada, H. Andou, Y. Moriyama, M. Maeda, *Optics Lett.* **14**, 987 (1989).

37. S.H. Bloom, E. Korevar, M. Rivers, C.S. Liu, *Optics Lett.* **15**, 294 (1990).

38. E.F. Palermo, S.R. Crouch, *Anal. Chem.* **45**, 1594 (1973).

39. J.A. Gelbwachs, *IEEE J. Quant. Elec.* **126**, 1140 (1990).

40. N.D. Finkelstein, W.R. Lempert, R.B. Miles, *Optics Lett.*, **22**, 537 (1997).

41. O.I. Matveev, B.W. Smith, J.D. Winefordner, *Optics Lett.*, **23**, 304 (1998).

42. O.I. Matveev, B.W. Smith, J.D. Winefordner, *Optics Commun.*, **156**, 259 (1998).

43. A.A. Podshivalov, W.L. Clevenger, O.I. Matveev, B.W. Smith, J.D. Winefordner, *Appl. Spectrosc.*, **54**, 175 (2000).

44. D. Pappas, O.I. Matveev, B.W. Smith, M.R. Shepard, A.A. Podshivalov, J.D. Winefordner, *Appl. Optics,* **39**, 4911 (2000).

45. E. Korovaar, M. Rivers, C.S. Liu, *Proc. SPIE*, **1059** 111 (1989).

46. S.M. Hamadani, J.A.D. Stockdale, R.N. Compton, M.S. Pindzola, *Phys. Rev. A*, **34**, 1938 (1986).

47. E.F. Palermo, S.R. Crouch, *Anal. Chem.*, **45**, 1594 (1973).

48. S.H. Bloom, P.A. Searcy, K. Choi, R. Kremer, E. Korevaar, *Opt. Lett.*, **18**, 244 (1993).

49. S.H. Bloom, R. Kremer, P.A. Searcy, M. Rivers, J. Menders, E. Korevaar, *Opt. Lett.*, **16**, 1794 (1991).

50. B. Yin, T.M. Shay, *Opt. Lett.*, **16**, 1617 (1991).

51. E.T. Dressler, A.G. Laux, R.I. Billmers, *J. Opt. Soc. Am. B*, **13**, 1849 (1996).

52. H. Chen, C.Y. She, P. Searcy, E. Korevaar, *Opt. Lett.*, **16**, 1617 (1991).

53. J. Menders, P. Searcy, K. Roff, E. Korevaar, *Opt. Lett.*, **17**, 1388 (1992).

54. J.A. Gelbwachs, *IEEE J. Quant. Elec.*, **26**, 1140 (1990).

55. Y. C. Chan, M.D. Tabat, J.A. Gelbwachs, *Opt. Lett.*, **14**, 722 (1989).

56. J.A. Gelbwachs, *Opt. Lett.*, **15**, 236 (1990).

57. D. Pappas, N.C. Pixley, O.I. Matveev, B.W. Smith, J.D. Winefordner, *Opt. Comm.*, **191**, 263 (2001)

58. D. Fink, S.N. Vodopia, *Appl. Optics*, **14**, 453 (1976).

59. O.I. Matveev, B. W. Smith, N. Omenetto, J. D. Winefornder, *Appl. Spectrosc.*, **53**, 1341 (1999).

60. J.D. Winefordner, I.B. Gornushkin, D. Pappas, O.I. Matveev, B.W. Smith, *J. Anal. Atom. Spec.*, **15**, 1161 (2000).

61. D. Pappas, N.C. Pixley, B.W. Smith, J.D. Winefornder, *Spectrochim. Acta Part B*, **56**, 1761 (2001).

62. R.L. Ott, *An Introduction to Statistical Methods and Data Analysis.*, 4th Ed., Danbury Press, New York (1988).

63. H. Shimizu, S.A. Lee, C.Y. She, *Appl. Optics*, **22**, 1373 (1983).

64. C.Y. She, R.J. Alvarez, L.M. Caldwell, D.A. Krueger, *Opt. Lett.*, **17**, 541 (1992).

65. Y. Wu, Y. Zhao, F. Yang, A. Xiong, J. Tang, L. Zheng, *Opt. Eng.*, **34**, 1195 (1995).

66. N.C. Pixley, T.L. Correll, D. Pappas, O.I. Matveev, B.W. Smith, J.D. Winefordner, *Applied Spectroscopy*, In Press.

67. N.C. Pixley, T.L. Correll, D. Pappas, O.I. Matveev, B.W. Smith, J.D. Winefordner, *Optics Letters*, **26**, 1946 (2001).

68. K.-J. Boller, A. Imamoglu, S.E. Harris, *Phys. Rev. Letters*, **66**, 2593 (1991).

69. D.J. Fulton, S. Shepherd, R.R. Mosely, B.D. Sinclair, M.H. Dunn, *Phys. Rev. A.*, **52**, 2302 (1995).

70. M. Mitsunaga, M. Yamashita, H. Inoue, *Phys. Rev. A.*, **62**, 013817-1 (2000).

71. J.R. Boon, E. Zekou, D. McGloin, M.H. Dunn, *Phys. Rev. A.*, **59**, 4675 (1999).

72. J.R. Boon, E. Zekou, D.J. Fulton, M.H. Dunn, *Phys. Rev. A.*, **57**, 1323 (1998)

73. P.S. Bhatia, G.R. Welch, M.O. Scully, *Opt. Comm*, **189**, 321 (2001)

74. C. Fort, F.S. Cataliotti, T.W. Hansch, M. Ignuscio, M. Prevedelli, *Opt. Comm.*, **139** 31 (1997)

BIOGRAPHICAL SKETCH

Dimitri Pappas was born in Elyria, Ohio, on November 19th, 1976. He is the second son of Greek immigrants Sotirios and Sotiria Pappas. His family moved to Ormond Beach, Florida in the summer of 1987. Dimitri attended the University of Florida in August 1995 and graduated in August of 1998 with a Bachelor of Science degree with a major in chemistry. Dimitri began his doctoral research in Dr. James D. Winefordner's laboratory at the University of Florida in August 1998.

I certify that I have read this study and that in my opinion it conforms to acceptable standards of scholarly presentation and is fully adequate, in scope and quality, as a dissertation for the degree of Doctor of Philosophy.

James D. Winefordner, Chair
Graduate Research Professor of Chemistry

I certify that I have read this study and that in my opinion it conforms to acceptable standards of scholarly presentation and is fully adequate, in scope and quality, as a dissertation for the degree of Doctor of Philosophy.

Robert T. Kennedy
Professor of Chemistry

I certify that I have read this study and that in my opinion it conforms to acceptable standards of scholarly presentation and is fully adequate, in scope and quality, as a dissertation for the degree of Doctor of Philosophy.

William Weltner, Jr.
Professor of Chemistry

I certify that I have read this study and that in my opinion it conforms to acceptable standards of scholarly presentation and is fully adequate, in scope and quality, as a dissertation for the degree of Doctor of Philosophy.

David H. Powell
Scientist of Chemistry

I certify that I have read this study and that in my opinion it conforms to acceptable standards of scholarly presentation and is fully adequate, in scope and quality, as a dissertation for the degree of Doctor of Philosophy.

Katherine N. Scott
Professor of Nuclear and Radiological Engineering

This dissertation was submitted to the Graduate Faculty of the Department of Chemistry in the College of Liberal Arts and Sciences and to the Graduate School and was accepted as partial fulfillment of the requirements for the degree of Doctor of Philosophy.

May 2002

Dean, Graduate School